https://doi.org/10.1016/j.compstruct.2021.113767

Comparisons of Nonlinear Vibrations among Pure Polymer Plate and Graphene Platelet Reinforced Composite Plates under Combined Transverse and Parametric Excitations

J. J. Mao[a,1], S. K. Lai[b,c,2], W. Zhang[a,3,*] and Y. Z. Liu[a,4]

[a]Beijing Key Laboratory of Nonlinear Vibrations and Strength of Mechanical Structures
Faculty of Materials and Manufacturing, Beijing University of Technology
Beijing 100124, P. R. China

[b]Department of Civil and Environmental Engineering, The Hong Kong Polytechnic University, Hong Kong, P. R. China

[c]Hong Kong Branch of National Rail Transit Electrification and Automation Engineering Technology Research Center, The Hong Kong Polytechnic University, Hong Kong, P. R. China

[1]Email: jiajia.mao@bjut.edu.cn, [2]Email: sk.lai@polyu.edu.hk

[3]Email: sandyzhang0@yahoo.com, [4]Email: liu_yaze@163.com

Running Headline: Comparisons of Nonlinear Vibrations among Pure Polymer and GRC Plates

[*]Corresponding author. E-mail address: sandyzhang0@yahoo.com

Abstract

The comparative researches of the nonlinear vibrations are obtained among the pure polymer plate and three types of graphene platelet reinforced polymer composite plates under combined the transverse and parametric excitations. All edges of the pure polymer and graphene platelet reinforced polymer composite plates are simply supported. Both the uniform and functionally graded distribution forms of the graphene platelets are considered. The differential governing equations of motion for the pure polymer and graphene platelet reinforced polymer composite plates are derived based on the first-order shear deformation plate theory, von Kármán strain displacement relationship and Hamilton principle. The fourth-order Galerkin truncation is employed to discretize the partial differential governing equations of motion to four-degree-of-freedom nonlinear dynamical system. The natural frequencies of the first four vibration modes are examined for the pure polymer and graphene platelet reinforced polymer composite plates with different geometric characteristics. In order to compare the nonlinear vibrations of the prestressed pure polymer and prestressed graphene platelet reinforced polymer composite plates subjected to the transverse point excitation and in-plane uniaxial/biaxial excitations, the time histories, phase portraits and Poincare maps are presented. Some validated results are conducted to present the accuracy of the present approach. The effects of the distribution forms and weight fractions of the graphene platelets on the nonlinear vibrations for the graphene platelet reinforced polymer composite plates are investigated in detail. The research results demonstrate that the nonlinear vibration behaviors of the prestressed pure polymer plate under the complex excitations can be remarkably stabilized by the reinforcement of the graphene platelets.

Keywords: Graphene platelet reinforced polymer composite plate; nonlinear vibrations; transverse and in-plane excitations; chaotic vibrations, four-degree-of-freedom nonlinear dynamical system

1. Introduction

The carbon-based composites have attracted huge research attentions and have become popular for a plenty of high-performance industrial applications due to their excellent mechanical strengths and functional properties, especially for carbon nanotube (CNT) reinforced polymer composite and graphene platelet reinforced polymer composite (GRC) [1-3]. The mechanical, thermal and electrical properties of CNT-reinforced composite and GRCs can be greatly enhanced due to the reinforcements of the CNTs and the graphene platelets (GPLs) [4-7]. The GPLs can lead to a superior enhancement than the CNTs as the two-dimensional (2D) attributes of GPLs can better improve the surface bonding among the matrix and reinforcing phases [6,7]. Meanwhile, more and more conventional materials are being replaced by the polymer composites for the lower cost, easier fabrication and better reproducibility of the polymer [1]. The GRC plates are promising to play an important role in different fields, such as aerospace science, electronic devices, energy storage, sensor and biomedical applications [8]. However, the different loads may cause some complex dynamic behaviors which could impact the effectiveness of the GRC pates during their services. In this paper, the comparative research of the free linear vibration, forced nonlinear vibration and parametrically excited nonlinear vibrations among the pure polymer rectangular plate and three different types of GRC plates are presented under different complex loadings.

In recent studies, Sun et al. [9] reported the axial Young's modulus of single-walled CNT arrays with a diameter from the nanometer to meter scales. Wang and Zhang [10] predicted the ameliorative mechanical properties of the CNT-reinforced composites through using the meshless method. Guo and Zhang [11] further studied the periodic and chaotic vibrations of the CNT-based polymer composite plates under various external forces. As the functionally graded materials (FGMs) can significantly improve the mechanical strength and thermal resistance to resist the deformation and damage [12-13], Shen [14] firstly formulated a constitutive model of the CNT-reinforced functionally graded composite (FG-CNTRC) plates.

Based on the pioneering study, Shen and his co-workers also investigated the dynamic responses [15] of the FG-CNTRC structures under the thermal-mechanical loads. Wang and his coworkers [16-18] considered the thermal-mechanical coupling effects, electro-mechanical coupling effects and fluid-solid interaction to study the nonlinear

dynamic characteristics of the FG plates. Zhang et al. [19-22] observed that the periodic vibrations of the FGM composite structures become chaotic vibrations under certain parametric conditions. In addition, Liang et al. [23] discussed the effect of the material distribution gradient index on the natural frequencies of the FGM curved pipes. Cao et al. [24] investigated the nonlinear vibrations of axially FGM beams by using an asymptotic development method. Considering the FGM plate with the axial compressed straight-sided loads, Zhang et al. [25,26] investigated the influences of the gradient index on the postbuckling behaviors of the FGM plate and laminated plate.

Furthermore, Ke et al. [27,28] studied the distribution effects of the CNTs on the nonlinear dynamics and stability of the FG-CNTRC beams. Besides, Liew and his associates also presented the comprehensive investigations for the nonlinear static and dynamic characteristics of the FG-CNTRC composite structures under various situations, for instance, the bending and vibrations of the FG-CNTRC laminated plates with the cracks [29-31], the vibrations of the FG-CNTRC quadrilateral plate [32-34], and active flutter control of the FG-CNTRC composite panels in the supersonic airflow [35]. Especially, they indicated that the FG distributed CNT reinforcements can help to reduce the amplitude of the impact response for the FG-CNTRC cylindrical shell [36].

Since the discovery of graphene [37], namely an allotrope of carbon in the form of a single layer of atoms, it has attracted considerable attentions in aerospace, mechanical, thermal, optical and electrical engineering fields. Rafiee and his colleagues [6] reported that Young's modulus of the epoxy nanocomposites can be significantly increased to 31% after adding a small weight fraction 0.1% of GPLs, but it can only be enhanced to 3% using the same weight fraction of CNTs. In addition, Zhao et al. [38] reported a significant enhancement of mechanical properties for the graphene-based polymer composites. More recently, Luong et al. [39] synthesized the gram-scale quantities of the graphene in less than one second from the inexpensive carbon sources, which will certainly facilitate the development of the GPL-reinforced composites.

From the perspective of the theoretical analysis, Zhang et al. [40,41] and Yan et al. [42] investigated the nonlinear vibration characteristics of the single-layered and bi-layered graphene sheets. Guo et al. [43] researched the nonlinear dynamic behaviors of the composite plate with the graphene skin. For the FG-GRC structures, Zhao et al. [44] presented a comprehensive review on the mechanical analyses of the FG-GRC structures. In the conclusion, the main research efforts of the FG-GRC structures are focused on the static problems and periodic vibration analyses [7,45-52]. There are few studies dealing

with the complex nonlinear vibration phenomena of the GRC structures even it will be exceedingly dangerous when the bifurcation and chaotic vibrations happen.

The present work investigates the natural frequencies and nonlinear vibrations of the pure polymer plates and GRC plates under combined the transverse and axial excitations. The partial differential governing equations of motion are formulated based on the first-order shear deformation plate theory, von Kármán nonlinear geometric relationship and Hamilton principle. The partial differential governing equations of motion are discretized by the fourth-order Galerkin truncation. We firstly check the natural frequencies of the first four vibration modes for the pure polymer plate and GRC plates with different geometric characteristics. Then, we give the comparison of the complex nonlinear vibrations, such as the period, bifurcation and chaotic vibrations, for the prestressed pure polymer plate and prestressed GRC plates subjected to different transverse and axial excitations. The effects of varying GPL weight fractions and distribution forms on the nonlinear vibrations are also investigated for the GRC plates under combined the transverse and axial excitations.

2. Theoretical Formulation

In Figure 1(a), a *K*-layered GRC plate with the length *a*, width *b* and thickness *h* is considered to investigate the vibration properties. All edges of the GRC plate are simply supported. A coordinate system is employed with *x*, *y* and *z* being in the length, width and thickness directions of the plate, respectively. The plate is subjected to the combination of the initial stresses q_1 and q_2, transverse point excitation $F(x,y,t)$ and in-plane excitations $q_x(x,y,t)$ and $q_y(x,y,t)$. Each GRC layer is made of a mixture of the rectangular GPL reinforcements and the polymer matrix. The thickness of each layer is identical, namely, $\Delta h = h/K$. It is assumed that the GPLs distribute uniformly in each GRC layer, but follow different distribution types, including the uniform (U) distribution and functionally graded (FG) forms, along the thickness of the plates. As shown in Figure 1(b-d), three different GPL distribution patterns are considered, namely, U, FG-X and FG-O patterns. The darker color demonstrates richer distribution of the GPLs in the GRC layer. To avoid the sudden variation of the material properties, the GPLs are assumed to distribute linear and symmetric along the mid-plane for the two different FG forms, namely, FG-X and FG-O patterns. The bottom and top layers of the FG-X GRC plate are

the GPLs richest, while the GPLs richest layers of the FG-O GRC plate are the middle layers.

The FG-X and FG-O GRC plates have the same values of the maximum and minimum GPL volume fractions, namely, $(KV^*)/2$ and V^*. The GPL volume content V_i of the i-th ($i = 1,2,\ldots,K$) GRC layers in the U, FG-X and FG-O GRC plates can be expressed as follows [45]

for U GRC plate

$$V_i = V_G, \tag{1}$$

for FG-X GRC plate

$$V_i = \left(\frac{N}{2} + 1 - i\right)V^* \quad \text{when} \quad i \le \frac{K}{2}, \tag{2a}$$

and

$$V_i = \left(i - \frac{N}{2}\right)V^* \quad \text{when} \quad i > \frac{K}{2}, \tag{2b}$$

for FG-O GRC plate

$$V_i = iV^* \quad \text{when} \quad i \le \frac{K}{2}, \tag{3a}$$

and

$$V_i = (N + 1 - i)V^* \quad \text{when} \quad i > \frac{K}{2}, \tag{3b}$$

with

$$V^* = \frac{2}{1 + \frac{K}{2}}V_G, \tag{4a}$$

and

$$V_G = \frac{g_G}{g_G + \frac{\rho_G}{\rho_M}(1 - g_G)}, \tag{4b}$$

where g_G is the weight fraction of the GPL reinforcements.

It is noticed that the GRC plate is turned to a pure polymer plate when the weight fraction g_G equals to zero. In order to calculate the effective Young modulus of the GRC plates, the modified Halpin-Tsai model [45] is employed. The rectangular GPL reinforcements with the length a_G, width b_G and thickness h_G are bonded perfectly to

the polymer matrix in each GRC layer. The effective Young modulus E_i of the *i*-th GRC layer is predicted by the effective Young modulus E_M of the polymer matrix and E_G of the GPLs

$$E_i = \frac{3}{8}\frac{1+\xi_L V_i}{1-\eta_L V_i}\times E_M + \frac{5}{8}\frac{1+\xi_W \eta_W V_i}{1-\eta_W V_i}\times E_M, \tag{5}$$

where

$$\eta_L = \frac{(E_G/E_M)-1}{(E_G/E_M)+\xi_L}, \quad \eta_W = \frac{(E_G/E_M)-1}{(E_G/E_M)+\eta_L}, \tag{6}$$

ξ_L and ξ_W respectively are the effects of the size and geometry of the GPL reinforcements [45]

$$\xi_L = 2\frac{l_G}{h_G}, \quad \xi_W = 2\frac{w_G}{h_G}. \tag{7}$$

In order to consider the mass density ρ and Poisson ratio ν of the *i*-th GRC layer, we adopt the rule of the mixture

$$\rho_i = \rho_G V_i + \rho_M (1-V_i), \tag{8a}$$

$$\nu_i = \nu_G V_i + \nu_M (1-V_i). \tag{8b}$$

Based on the mid-plane displacements $U(x,y,t)$, $V(x,y,t)$, $W(x,y,t)$, $\varphi_x(x,y,t)$ and $\varphi_y(x,y,t)$ of the GRC plate, the displacements u_1, u_2 and u_3 for an arbitrary point of the GRC plate in the *x*, *y* and *z* directions are respectively expressed in accordance with the first-order shear deformation plate theory [45]

$$u_1(x,y,z,t) = U(x,y,t) + z\varphi_x(x,y,t), \tag{9a}$$

$$u_2(x,y,z,t) = V(x,y,t) + z\varphi_y(x,y,t), \tag{9b}$$

$$u_3(x,y,z,t) = W(x,y,t), \tag{9c}$$

where *t* is time.

Therefore, von Kármán strain-displacement relationship is given as

$$\begin{Bmatrix} \varepsilon_{xx} \\ \varepsilon_{yy} \\ \gamma_{xz} \\ \gamma_{yz} \\ \gamma_{xy} \end{Bmatrix} = \begin{Bmatrix} \varepsilon_{xx}^{(0)} \\ \varepsilon_{yy}^{(0)} \\ \gamma_{xz}^{(0)} \\ \gamma_{yz}^{(0)} \\ \gamma_{xy}^{(0)} \end{Bmatrix} + z \begin{Bmatrix} \varepsilon_{xx}^{(1)} \\ \varepsilon_{yy}^{(1)} \\ \gamma_{xz}^{(1)} \\ \gamma_{yz}^{(1)} \\ \gamma_{xy}^{(1)} \end{Bmatrix} = \begin{Bmatrix} \dfrac{\partial U}{\partial x} + \dfrac{1}{2}\left(\dfrac{\partial W}{\partial x}\right)^2 \\ \dfrac{\partial V}{\partial y} + \dfrac{1}{2}\left(\dfrac{\partial W}{\partial y}\right)^2 \\ \dfrac{\partial W}{\partial x} + \varphi_x \\ \dfrac{\partial W}{\partial y} + \varphi_y \\ \dfrac{\partial U}{\partial y} + \dfrac{\partial V}{\partial x} + \dfrac{\partial W}{\partial x}\dfrac{\partial W}{\partial y} \end{Bmatrix} + z \begin{Bmatrix} \dfrac{\partial \varphi_x}{\partial x} \\ \dfrac{\partial \varphi_y}{\partial y} \\ 0 \\ 0 \\ \dfrac{\partial \varphi_x}{\partial y} + \dfrac{\partial \varphi_y}{\partial x} \end{Bmatrix}, \tag{10}$$

where ε_{xx} and ε_{yy} are respectively the normal strains along the *x*- and the *y*-axes, and γ_{xy}, γ_{yz} and γ_{xz} are respectively the shear strains along the *xy*, *yz* and *xz* planes.

According to the nonlinear strain-displacement relationship given in equation (10), the normal stresses σ_{xx} and σ_{yy} and shear stresses σ_{xy}, σ_{yz} and σ_{xz} of the *i*-th GRC layer are written as

$$\begin{Bmatrix} \sigma_{xx} \\ \sigma_{yy} \\ \sigma_{xy} \\ \sigma_{yz} \\ \sigma_{xz} \end{Bmatrix}_{(i)} = \begin{bmatrix} Q_{11} & Q_{12} & 0 & 0 & 0 \\ Q_{12} & Q_{22} & 0 & 0 & 0 \\ 0 & 0 & Q_{66} & 0 & 0 \\ 0 & 0 & 0 & Q_{44} & 0 \\ 0 & 0 & 0 & 0 & Q_{55} \end{bmatrix}_{(i)} \begin{Bmatrix} \varepsilon_{xx} \\ \varepsilon_{yy} \\ 2\varepsilon_{xy} \\ 2\varepsilon_{yz} \\ 2\varepsilon_{xz} \end{Bmatrix}_{(i)}, \tag{11}$$

where $i = 1,2,\cdots,N$, and

$$Q_{11_{(i)}} = Q_{22_{(i)}} = \frac{E_i}{1-\nu_i^2}, \quad Q_{12_{(i)}} = \frac{\nu_i E_i}{1-\nu_i^2}, \quad Q_{44_{(i)}} = Q_{55_{(i)}} = Q_{66_{(i)}} = \frac{\nu_i E_i}{2(1+\nu_i)}. \tag{12}$$

The in-plane harmonic excitations $q_x(x,y,t)$ and $q_y(x,y,t)$ are expressed in the following forms

$$q_x(x,y,z) = q_{x0}\cos(\Omega_1 t), \tag{13a}$$

and

$$q_y(x,y,t) = q_{y0}\cos(\Omega_2 t), \tag{13b}$$

where q_{x0} and q_{y0} are the amplitudes of the in-plane distributed harmonic excitations along the *x* and *y* directions, respectively.

The transverse harmonic excitation at the point (x_0, y_0) on the upon surface of GRC plate is expressed as

$$F(x,y,t)=F_0\,\delta(x-x_0)\delta(y-y_0)\cos(\Omega_3 t), \tag{14}$$

where F_0 is the amplitude of the transverse point excitation and δ is Dirac-delta function.

Based on Hamilton principle, the partial differential governing equations of motion for the GRC plates subjected to the initial stresses and the harmonic excitations along the transverse and in-plane directions are obtained as follows

$$\frac{\partial N_x}{\partial x}+\frac{\partial N_{xy}}{\partial y}=I_0\ddot{U}, \tag{15a}$$

$$\frac{\partial N_y}{\partial y}+\frac{\partial N_{xy}}{\partial x}=I_0\ddot{V}, \tag{15b}$$

$$\frac{\partial}{\partial x}\left(N_x\frac{\partial w}{\partial x}+N_{xy}\frac{\partial w}{\partial y}\right)+\frac{\partial}{\partial y}\left(N_y\frac{\partial w}{\partial y}+N_{xy}\frac{\partial w}{\partial x}\right)+\frac{\partial Q_x}{\partial x}+\frac{\partial Q_y}{\partial y}+F(x,y,t)=I_0\ddot{W}+c\dot{W}, \tag{15c}$$

$$\frac{\partial M_x}{\partial x}+\frac{\partial M_{xy}}{\partial y}-Q_x=I_2\ddot{\varphi}_x, \tag{15d}$$

$$\frac{\partial M_y}{\partial y}+\frac{\partial M_{xy}}{\partial x}-Q_y=I_2\ddot{\varphi}_y, \tag{15e}$$

where c is the damping coefficient, I_j ($j=0,2$) are the inertia related terms

$$I_j=\sum_{i=1}^{N}\int_{z_i}^{z_{i+1}} z^j\rho_i dz. \tag{16}$$

The axial forces N_x, N_y and N_{xy}, bending moments M_x, M_y and M_{xy} and shear forces Q_x and Q_y are written as follows

$$\begin{Bmatrix}N_x\\N_y\\N_{xy}\end{Bmatrix}=\begin{bmatrix}A_{11}&A_{12}&0\\A_{12}&A_{22}&0\\0&0&A_{66}\end{bmatrix}\begin{Bmatrix}\varepsilon_{xx}^{(0)}\\\varepsilon_{yy}^{(0)}\\\gamma_{xy}^{(0)}\end{Bmatrix}-\begin{Bmatrix}q_1+q_{x0}\cos(\Omega_1 t)\\q_2+q_{y0}\cos(\Omega_2 t)\\0\end{Bmatrix}h, \tag{17a}$$

$$\begin{Bmatrix}M_x\\M_y\\M_{xy}\end{Bmatrix}=\begin{bmatrix}D_{11}&D_{12}&0\\D_{12}&D_{22}&0\\0&0&D_{66}\end{bmatrix}\begin{Bmatrix}\varepsilon_{xx}^{(1)}\\\varepsilon_{yy}^{(1)}\\\gamma_{xy}^{(1)}\end{Bmatrix}, \tag{17b}$$

$$\begin{Bmatrix}Q_y\\Q_x\end{Bmatrix}=\begin{bmatrix}A_{44}&0\\0&A_{55}\end{bmatrix}\begin{Bmatrix}\gamma_{yz}^{(0)}\\\gamma_{xz}^{(0)}\end{Bmatrix}, \tag{17c}$$

where the stiffness components A_{ij} and D_{ij} are given by

$$\left(A_{ij}, D_{ij}\right)=\sum_{k=1}^{N}\int_{z_k}^{z_{k+1}}\left(1, z^2\right)Q_{ij_{(k)}}dz\,,\ (i,j=1,2,6),\tag{18a}$$

$$A_{ij}=K_s\sum_{k=1}^{N}\int_{z_k}^{z_{k+1}}Q_{ij_{(k)}}dz\,,\ (i,j=4,5),\tag{18b}$$

and the shear correction factor $K_s=5/6$.

Introducing the following dimensionless parameters, we have

$$\{\zeta,\xi\}=\left\{\frac{x}{a},\frac{y}{b}\right\},\ \{\zeta_0,\xi_0\}=\left\{\frac{x_0}{a},\frac{y_0}{a}\right\},\ \{u,v,w\}=\left\{\frac{U}{h},\frac{V}{h},\frac{W}{h}\right\},\ \eta=\frac{a}{h},\ \lambda=\frac{a}{b},\tag{19a}$$

$$\overline{A}_{ij}=\frac{A_{ij}}{A_{110}},\ \overline{D}_{ij}=\frac{D_{ij}}{A_{110}h^2},\ \left\{\bar{I}_0,\bar{I}_2\right\}=\left\{\frac{I_0}{I_{10}},\frac{I_2}{I_{10}h^2}\right\},\ A_{110}=E_M h,\ I_{10}=\rho_M h,$$

$$\overline{q}_1=\frac{q_1 h}{A_{110}},\ \overline{q}_2=\frac{q_2 h}{A_{110}},\ \overline{q}_{x0}=\frac{q_{x0}h}{A_{110}},\ \overline{q}_{y0}=\frac{q_{y0}h}{A_{110}},\ \overline{F}_0=\frac{F_0}{bA_{110}},$$

$$\tau=\frac{t}{a}\sqrt{\frac{A_{110}}{I_{10}}},\ \overline{\Omega}_i=a\Omega_i\sqrt{\frac{I_{10}}{A_{110}}},\ \overline{c}=\frac{ac}{\sqrt{I_{10}\cdot A_{110}}}.\tag{19b}$$

Substituting equation (17) into equation (15), the partial differential governing equation of motion for the prestressed GRC plates subjected to the complex excitations can be rewritten in the dimensionless form

$$\overline{A}_{11}\left(\frac{\partial^2 u}{\partial\zeta^2}+\frac{1}{\eta}\frac{\partial w}{\partial\zeta}\frac{\partial^2 w}{\partial\zeta^2}\right)+\overline{A}_{12}\left(\lambda\frac{\partial^2 v}{\partial\zeta\partial\xi}+\frac{\lambda^2}{\eta}\frac{\partial w}{\partial\xi}\frac{\partial^2 w}{\partial\zeta\partial\xi}\right)$$
$$+\overline{A}_{66}\left(\lambda^2\frac{\partial^2 u}{\partial\xi^2}+\lambda\frac{\partial^2 v}{\partial\zeta\partial\xi}+\frac{\lambda^2}{\eta}\frac{\partial w}{\partial\xi}\frac{\partial^2 w}{\partial\zeta\partial\xi}+\frac{\lambda^2}{\eta}\frac{\partial w}{\partial\zeta}\frac{\partial^2 w}{\partial\xi^2}\right)=\bar{I}_0\ddot{u}\,,\tag{20a}$$

$$\overline{A}_{12}\left(\lambda\frac{\partial^2 u}{\partial\zeta\partial\xi}+\frac{\lambda}{\eta}\frac{\partial w}{\partial\zeta}\frac{\partial^2 w}{\partial\zeta\partial\xi}\right)+\overline{A}_{22}\left(\lambda^2\frac{\partial^2 u}{\partial\xi^2}+\frac{\lambda^3}{\eta}\frac{\partial w}{\partial\xi}\frac{\partial^2 w}{\partial\xi^2}\right)$$
$$+\overline{A}_{66}\left(\lambda\frac{\partial^2 u}{\partial\zeta\partial\xi}+\frac{\partial^2 v}{\partial\zeta^2}+\frac{\lambda}{\eta}\frac{\partial w}{\partial\xi}\frac{\partial^2 w}{\partial\zeta^2}+\frac{\lambda}{\eta}\frac{\partial w}{\partial\zeta}\frac{\partial^2 w}{\partial\zeta\partial\xi}\right)=\bar{I}_0\ddot{v}\,,\tag{20b}$$

$$\overline{Z}_1+\overline{Z}_2+\overline{A}_{55}\left(\lambda^2\frac{\partial^2 w}{\partial\xi^2}+\lambda\eta\frac{\partial\varphi_y}{\partial\xi}\right)+\overline{A}_{44}\left(\lambda^2\frac{\partial^2 w}{\partial\zeta^2}+\eta\frac{\partial\varphi_x}{\partial\zeta}\right)-\left[\overline{q}_1+\overline{q}_{x0}\cos\left(\overline{\Omega}_1\tau\right)\right]\frac{\partial^2 w}{\partial\zeta^2}$$
$$-\left[\overline{q}_2+\overline{q}_{y0}\cos\left(\overline{\Omega}_2\tau\right)\right]\frac{\partial^2 w}{\partial\xi^2}+\eta\,f(\zeta,\xi)\cos\left(\overline{\Omega}_3\tau\right)=\bar{I}_0\ddot{w}+\overline{c}\dot{w}\,,\tag{20c}$$

$$\overline{D}_{11}\frac{\partial^2\varphi_x}{\partial\zeta^2}+\overline{D}_{12}\lambda\frac{\partial^2\varphi_y}{\partial\zeta\partial\xi}+\overline{D}_{66}\left(\lambda^2\frac{\partial^2\varphi_x}{\partial\xi^2}+\lambda\frac{\partial^2\varphi_y}{\partial\zeta\partial\xi}\right)-\overline{A}_{44}\left(\eta\frac{\partial w}{\partial\zeta}+\eta^2\varphi_x\right)+=\bar{I}_2\ddot{\varphi}_x\,,\tag{20d}$$

$$\overline{D}_{12}\lambda\frac{\partial^2\varphi_x}{\partial\zeta\partial\xi}+\overline{D}_{22}\lambda^2\frac{\partial^2\varphi_y}{\partial\xi^2}+\overline{D}_{66}\left(\lambda\frac{\partial^2\varphi_x}{\partial\zeta\partial\xi}+\frac{\partial^2\varphi_y}{\partial\zeta^2}\right)-\overline{A}_{55}\left(\eta\lambda\frac{\partial w}{\partial\xi}+\eta^2\varphi_y\right)=\bar{I}_2\ddot{\varphi}_y, \quad (20e)$$

where the dimensionless nonlinear terms $\overline{Z}_1$ and $\overline{Z}_2$ are presented in the Appendix A, and the transverse point excitation is given

$$f(\zeta,\xi)=\overline{F}_0\,\delta(\zeta-\zeta_0)\,\delta(\xi-\xi_0). \quad (21)$$

3. Solution Procedure

Since all edges of the GRC plates are simply supported, the dimensionless mid-plane displacements $u(\zeta,\xi,\tau)$, $v(\zeta,\xi,\tau)$, $w(\zeta,\xi,\tau)$, $\varphi_x(\zeta,\xi,\tau)$ and $\varphi_y(\zeta,\xi,\tau)$ of the GRC plates are satisfied by the following solution forms

$$u(\zeta,\xi,\tau)=\sum_{m=1}^{M}\sum_{n=1}^{N}u_{mn}(\tau)\cos(m\pi\zeta)\sin(n\pi\zeta), \quad (22a)$$

$$v(\zeta,\xi,\tau)=\sum_{m=1}^{M}\sum_{n=1}^{N}v_{mn}(\tau)\sin(m\pi\zeta)\cos(n\pi\zeta), \quad (22b)$$

$$w(\zeta,\xi,\tau)=\sum_{m=1}^{M}\sum_{n=1}^{N}w_{mn}(\tau)\sin(m\pi\zeta)\sin(n\pi\zeta), \quad (22c)$$

$$\varphi_x(\zeta,\xi,\tau)=\sum_{m=1}^{M}\sum_{n=1}^{N}\varphi_{x,mn}(\tau)\cos(m\pi\zeta)\sin(n\pi\zeta), \quad (22d)$$

$$\varphi_y(\zeta,\xi,\tau)=\sum_{m=1}^{M}\sum_{n=1}^{N}\varphi_{y,mn}(\tau)\cos(m\pi\zeta)\sin(n\pi\zeta), \quad (22e)$$

where m and n are respectively the number of the axial half waves and transverse half waves in the mode shape, M and N respectively represent the total mode expansion terms along the ξ- and ζ- axes, and $u_{mn}(\tau)$, $v_{mn}(\tau)$, $w_{mn}(\tau)$, $\varphi_{x,mn}(\tau)$ and $\varphi_{y,mn}(\tau)$ are the discretized displacements which are the functions of the dimensionless time τ.

Noticing the transverse point excitation $f(\zeta,\xi)$ in equation (21) can be expanded in a series form as

$$f(\zeta,\xi)=\sum_{m=1}^{M}\sum_{n=1}^{N}f_{mn}(\tau)\sin(m\pi\zeta)\sin(n\pi\zeta), \quad (23)$$

where

$$f_{mn}=4\overline{F}_0\sin(m\pi\zeta_0)\sin(n\pi\xi_0), \quad (24)$$

Nosier and Reddy [53] proved that the in-plane and rotation inertia terms barely affect the nonlinear dynamic behaviors of the simply-supported plates. Yao and Zhang [54] also demonstrated that the first four vibration modes of the simply-supported plate are sufficiently accurate to dominate the vibration amplitudes of these plates. Therefore, we ignore all inertia terms of the in-plane and rotations. To deal with equation (20), the fourth-order Galerkin truncation, namely, $M = N = 2$, is introduced.

Substituting equations (22) and (23) into equation (20), multiplying them by $\cos(p\pi\zeta)\sin(q\pi\xi)$, $\sin(p\pi\zeta)\cos(q\pi\xi)$, $\sin(p\pi\zeta)\sin(q\pi\xi)$, $\cos(p\pi\zeta)\sin(q\pi\xi)$ and $\sin(p\pi\zeta)\cos(q\pi\xi)$, respectively, then, integrating the resulting equations with respect to ζ from 0 to 1 and ξ from 0 to 1, the dimensionless discretized in-plane and rotation displacements can be represented by the dimensionless discretized transverse displacements. Therefore, we derive four-degree-of-freedom nonlinear governing equations of motion for the GRC plates

$$\ddot{w}_{11} + \mu_1\dot{w}_{11} + \left[\omega_{11}^2 + a_7 q_{x0}\cos\left(\overline{\Omega}_1\tau\right) + a_8 q_{y0}\cos\left(\overline{\Omega}_2\tau\right)\right] w_{11} + a_1 w_{12}w_{21}w_{22} + a_2 w_{11}w_{12}^2 + a_3 w_{11}w_{21}^2 + a_4 w_{11}w_{22}^2 + a_5 w_{11}^3 = a_6 F_0\sin(\pi\zeta_0)\sin(\pi\xi_0)\cos\left(\overline{\Omega}_3\tau\right), \quad (25a)$$

$$\ddot{w}_{12} + \mu_2\dot{w}_{12} + \left[\omega_{12}^2 + b_7 q_{x0}\cos\left(\overline{\Omega}_1\tau\right) + b_8 q_{y0}\cos\left(\overline{\Omega}_2\tau\right)\right] w_{12} + b_1 w_{11}w_{21}w_{22} + b_2 w_{12}w_{11}^2 + b_3 w_{12}w_{21}^2 + b_4 w_{12}w_{22}^2 + b_5 w_{12}^3 = b_6 F_0\sin(\pi\zeta_0)\sin(2\pi\xi_0)\cos\left(\overline{\Omega}_3\tau\right), \quad (25b)$$

$$\ddot{w}_{21} + \mu_3\dot{w}_{21} + \left[\omega_{21}^2 + c_7 q_{x0}\cos\left(\overline{\Omega}_1\tau\right) + c_8 q_{y0}\cos\left(\overline{\Omega}_2\tau\right)\right] w_{21} + c_1 w_{11}w_{12}w_{22} + c_2 w_{21}w_{11}^2 + c_3 w_{21}w_{12}^2 + c_4 w_{21}w_{22}^2 + c_5 w_{21}^3 = c_6 F_0\sin(2\pi\zeta_0)\sin(\pi\xi_0)\cos\left(\overline{\Omega}_3\tau\right), \quad (25c)$$

$$\ddot{w}_{22} + \mu_4\dot{w}_{22} + \left[\omega_{22}^2 + d_7 q_{x0}\cos\left(\overline{\Omega}_1\tau\right) + d_8 q_{y0}\cos\left(\overline{\Omega}_2\tau\right)\right] w_{22} + d_1 w_{11}w_{12}w_{21} + d_2 w_{22}w_{11}^2 + d_3 w_{22}w_{12}^2 + d_4 w_{22}w_{21}^2 + d_5 w_{22}^3 = d_6 F_0\sin(2\pi\zeta_0)\sin(2\pi\xi_0)\cos\left(\overline{\Omega}_3\tau\right), \quad (25d)$$

where "$\cdot$" and "$\cdot\cdot$" denote the first- and second-order derivatives with respect to the dimensionless time variable τ, ω_{11}, ω_{12}, ω_{21} and ω_{22} are the dimensionless natural frequencies of the first four vibration modes for the GRC plate with the initial stresses q_1 and q_2, $\mu_i\,(i=1-4)$, $a_i\,(i=1-4)$, $b_i\,(i=1-4)$, $c_i\,(i=1-4)$ and $d_i\,(i=1-4)$ are the constants and depend on the characteristics of the system.

For simplicity, we only give some brief expressions as follows

$$\mu_1 = \mu_2 = \mu_3 = \mu_4 = \frac{\overline{c}}{\overline{I}_0}, a_6 = b_6 = c_6 = d_6 = \frac{4\eta}{\overline{I}_0}, \quad a_7 = b_7 = -\frac{\pi^2}{\overline{I}_0},$$

$$c_7 = d_7 = -\frac{4\pi^2}{\bar{I}_0},\quad a_8 = c_8 = -\frac{(\pi\lambda)^2}{\bar{I}_0},\quad b_8 = d_8 = -\frac{(2\pi\lambda)^2}{\bar{I}_0}. \tag{26}$$

Let $x_1 = w_{11}$, $x_3 = w_{12}$, $x_5 = w_{21}$, $x_7 = w_{22}$, equation (25) can be written as an eight-dimensional nonlinear dynamical system

$$x_2 = \dot{x}_1, \tag{27a}$$

$$\dot{x}_2 = -\mu_1 x_2 - \left[\omega_1^2 + a_7 q_{x0}\cos(\overline{\Omega}_1\tau) + a_8 q_{y0}\cos(\overline{\Omega}_2\tau)\right] x_1 - a_1 x_3 x_5 x_7 - a_2 x_1 x_3^2 - a_3 x_1 x_5^2 - a_4 x_1 x_7^2 - a_5 x_1^3 + a_6 F_0 \sin(\pi\zeta_0)\sin(\pi\xi_0)\cos(\overline{\Omega}_3\tau), \tag{27b}$$

$$x_4 = \dot{x}_3, \tag{27c}$$

$$\dot{x}_4 = -\mu_2 x_4 - \left[\omega_2^2 + b_7 q_{x0}\cos(\overline{\Omega}_1\tau) + b_8 q_{y0}\cos(\overline{\Omega}_2\tau)\right] x_3 - b_1 x_1 x_5 x_7 - b_2 x_3 x_1^2 - b_3 x_3 x_5^2 - b_4 x_3 x_7^2 - b_5 x_3^3 + b_6 F_0 \sin(\pi\zeta_0)\sin(2\pi\xi_0)\cos(\overline{\Omega}_3\tau), \tag{27d}$$

$$x_6 = \dot{x}_5, \tag{27e}$$

$$\dot{x}_6 = -\mu_3 x_6 - \left[\omega_3^2 + c_7 q_{x0}\cos(\overline{\Omega}_1\tau) + c_8 q_{y0}\cos(\overline{\Omega}_2\tau)\right] x_5 - c_1 x_1 x_3 x_7 - c_2 x_5 x_1^2 - c_3 x_5 x_3^2 - c_4 x_5 x_7^2 - c_5 x_5^3 + c_6 F_0 \sin(2\pi\zeta_0)\sin(\pi\xi_0)\cos(\overline{\Omega}_3\tau), \tag{27f}$$

$$x_8 = \dot{x}_7, \tag{27g}$$

$$\dot{x}_8 = -\mu_4 x_8 - \left[\omega_4^2 + d_7 q_{x0}\cos(\overline{\Omega}_1\tau) + d_8 q_{y0}\cos(\overline{\Omega}_2\tau)\right] x_7 - d_1 x_1 x_3 x_5 - d_2 x_7 x_1^2 - d_3 x_7 x_3^2 - d_4 x_7 x_5^2 - d_5 x_7^3 + d_6 F_0 \sin(2\pi\zeta_0)\sin(2\pi\xi_0)\cos(\overline{\Omega}_3\tau). \tag{27h}$$

In the following analysis, equation (27) is used to numerically investigate the natural frequencies and nonlinear vibration characteristics of the pure polymer plate and GRC plates.

To validate the present research, a square graphene reinforced epoxy composite plate is considered with $0.45\,\text{m}\times 0.45\,\text{m}\times 0.045\,\text{m}$ and the weight fraction of the GPL reinforcement $g_G = 1\%$ [45]. Table 1 gives the dimensionless natural frequencies ($\Omega h\sqrt{\rho_M / E_M}$) of the GRC plates with different GPL distribution patterns. Song et al.'s results [48] are also listed in Table 1. It is observed that the present results are in good agreement with the available solutions [48]. It is also demonstrated that the dimensionless natural frequencies of the higher mode vibrations are significantly larger than these of the lower modes. Specifically, the fifth order dimensionless natural frequency is larger than the first four order dimensionless foundation frequencies. Besides, the low frequency

vibrations are the key impact for the stability of the structures. Therefore, only the first four vibration modes of the GRC plates are considered, namely, $M = N = 2$.

4. Comparative Researches

4.1 Comparisons of Natural Frequency

In this section, the parametric analyses are conducted to compare the nonlinear vibrations among the pure polymer plate and GRC plates under different external and axial excitations. The effects of the geometric characteristics for these plates, distribution forms and weight fractions of the GPLs on the nonlinear vibration responses are studied. For the polymer matrix, we choose an epoxy material which has the material properties $E_M = 3.0\,\text{GPa}$, $\rho_M = 1.2\,\text{g/cm}^3$ and $v_M = 0.34$ [45]. The material properties of the GPLs are $E_G = 3.0\,\text{GPa}$, $\rho_G = 1.06\,\text{g/cm}^3$ and $v_M = 0.186$ [45].

Unless otherwise stated in this study, the square plates are considered. A weight fraction 0.5% for the GPL reinforcements is involved in the GRC plates with the thickness h = 0.01m. The length, width and thickness of the GPLs are $2.5\mu\text{m}$, $1.5\mu\text{m}$ and 1.5 nm, respectively. The total number of the layers in the GRC plate is K = 10. In addition, the dimensionless frequencies of the harmonic excitations are $\overline{\Omega}_1 = \overline{\Omega}_2 = \overline{\Omega}_3 = 0.6$.

Ignoring the initial stresses q_1 and q_2, Figure 2 presents the effects of the length a for the plates on the first four dimensionless natural frequencies ω_{11}, ω_{12}, ω_{21} and ω_{22} of the pure epoxy plate and GRC plates with the U, FG-X and FG-O distribution patterns. It is seen that the curves of the second-order and third-order dimensionless natural frequencies are coincident because all plates are square. For a given length a, the reinforcement of the GPLs significantly increases the natural frequencies of the epoxy plate. The FG-X GRC plate has the largest natural frequencies, and the natural frequencies of the U GRC plate are bigger than that of the FG-O GRC plate. It is because the GPLs can improve the stiffness of the epoxy plate, and the FG-X distribution pattern performs the best effectiveness. Besides, with the increase of the length a, the stiffness terms of the pure epoxy plate and GRC plates are reducing, which result in the decrease of the dimensionless natural frequencies. In order to specifically compare the nonlinear vibrations among the pure epoxy plate and GRC plates, the prestressed pure polymer plate

and prestressed GRC plates subjected to different excitations are considered with $a = b = 0.2\,\mathrm{m}$.

4.2 Comparisons of Forced Vibrations

In this subsection, the initial stresses q_1 and q_2 are considered as 10^5 N/m^2. The transverse point excitation $f(\zeta, \xi)$ placed on the point $(\zeta_0, \xi_0) = (1/3, 1/3)$ subjects to the prestressed plates, and the in-plane excitations are ignored. In order to analyze the different nonlinear vibration behaviors of the GRC plates with different GPL distribution patterns, the damping coefficient must be defined as it has the important influence on the nonlinear dynamics of the plates. Figure 3 presents the bifurcation diagrams of the first-order vibration mode for the prestressed pure epoxy plate with $F_0 = 9000\,\mathrm{N}$ when the dimensionless damping coefficient $\bar{c}$ increases from 0 to 0.04. The corresponding two-dimensional phase portraits with Poincaré maps of the first-order vibration mode are also given when the dimensionless damping coefficients respectively are $\bar{c} = 0.005$, $\bar{c} = 0.015$ and $\bar{c} = 0.03$, as shown in Figure 3. It can be seen that as the increases of the dimensionless damping coefficient, the nonlinear dynamical system changes from the chaotic to quasi-periodic vibrations and finally turns to the period vibrations.

In order to indicate the enhanced effects of the nonlinear vibrations for the prestressed pure epoxy plate by the GPL reinforcements, the dimensionless damping coefficient $\bar{c} = 0.006$ is selected in the following analyses. Figures 4-7 compare the periodic and chaotic vibration regions as well as the vibration amplitudes among the pressed pure epoxy plate and three types of GRC plates. As the third-order vibration modes for these plates have the same performances as those of the second-order vibration modes, only the first-order, second-order and forth-order vibration modes are given below.

Figure 4 illustrates the bifurcation diagrams of the prestressed pure epoxy plate, prestressed U, FG-X and FG-O GRC plates. It is observed that the periodic, quasi-periodic and chaotic vibrations appear alternately for the prestressed pure epoxy plate and prestressed GRC plates when the transverse point excitation F_0 is located in the range of (0, 30kN). It is found from Figure 4(a), 4(c) and 4(e) that the chaotic vibrations occur in the prestressed pure epoxy plate when the transverse point excitation F_0 is located in the ranges of [3.78kN, 5.94kN], [7.32kN, 10.38kN] and [19.08kN, 19.20kN]. In the intervals [12.24kN, 13.56kN] and [15.30kN, 15.90kN], some small periodic windows exist for the

prestressed pure epoxy plate. Based on Figure 4(b), 4(d) and 4(f), the chaotic vibrations respectively happen in the prestressed U, FG-O and FG-X GRC plates when the transverse point excitation F_0 is located in the ranges of [14.94kN, 16.56kN], [20.58kN, 21.96kN] and [26.40kN, 27.30kN]. These imply that the GPLs can postpone the occurrence of the chaotic vibrations for the typical prestressed pure epoxy plate. Furthermore, the prestressed FG-X GRC plate has the most stable vibration property.

When the amplitude of the transverse point excitation is $F_0 = 9428\,\mathrm{N}$, the time histories and two-dimensional phase portraits with Poincaré maps of the first-order, second-order and forth-order vibration modes for the prestressed pure epoxy plate are presented, as shown in Figure 5. It is seen that the prestressed pure epoxy plate has the chaotic vibrations. Figures 6 presents the vibration properties of the first-order, second-order and forth-order vibration modes for the prestressed U GRC plate. As the reinforcement caused by the GPLs, the U GRC plate has the periodic vibration.

When the amplitude of the transverse point excitation is $F_0 = 9428\,\mathrm{N}$, the time histories, two-dimensional phase portraits with Poincaré maps as well as three-dimensional phase portraits are represented for the first-order vibration modes of the prestressed FG-X and FG-O GRC plates, as shown in Figure 7. Like the prestressed U GRC plate, both of the prestressed FG-X and FG-O GRC plates have the periodic vibrations. Comparing Figure 7 with Figure 6, it is known that the prestressed FG-X GRC plate has the smallest vibration amplitude. The prestressed FG-O GRC plate has the largest vibration amplitude. Nevertheless, the vibration of the prestressed U GRC plate is located between the smallest and largest vibrations in the prestressed FG-X and FG-O GRC plates.

In order to further compare the vibration amplitudes of the prestressed pure epoxy plate and GRC plates with different GPL distribution patterns, Table 2 lists the first-order, second-order and forth-order vibration amplitudes of the prestressed pure epoxy plate and GRC plates subjected to varying transverse point excitation. It is seen that all first-order vibration amplitudes of the prestressed GRC plates with different GPL distribution patterns are obviously lower than the first-order vibration amplitudes of the prestressed pure epoxy plate. Generally, the vibration properties of the structures depend on the first-order mode vibration. Therefore, the vibration amplitudes of the prestressed pure epoxy plate can be significantly reduced by the GPL reinforcements. Among the first-order mode vibration amplitudes of three types of the prestressed GRC plates with

different GPL distribution patterns, the pressed X GRC plate always has the lowest vibration amplitude. Thus, the vibration behaviors of the prestressed pure epoxy plate can be best improved by the X distributed GPL reinforcements.

In Figure 8, the bifurcation diagrams of four first-order vibration modes are represented for the prestressed pure epoxy plate, prestressed U, FG-X and FG-O GRC plates when the transverse point excitation subjects to different positions. The black, blue and red colors respectively represent the positions (ζ_0, ξ_0) = (1/3, 1/3), (1/3, 1/2) and (1/2, 1/2). In Figure 9(a), the chaotic vibrations firstly happen in the prestressed pure epoxy plate for the transverse point excitation subjecting to the positions (ζ_0, ξ_0) = (1/3, 1/3) and (1/3, 1/2) when the amplitude F_0 of the transverse point excitation is around 3.78kN. When $(\zeta_0, \xi_0) = (1/2, 1/2)$, the chaotic vibrations are excited when the amplitude F_0 of the transverse point excitation increases to 11.04kN. As shown in Figures 8(b) and 8(c), when $(\zeta_0, \xi_0) = (1/2, 1/2)$, the chaotic vibrations cannot be excited for the prestressed U and FG-X GRC plates even if the amplitude F_0 of the transverse point excitation increases to 30kN. In Figure 8(d), the chaotic vibrations of the prestressed FG-O GRC plate for $(\zeta_0, \xi_0) = (1/3, 1/2)$, (1/3, 1/3) and (1/2, 1/2) are respectively excited when the amplitudes F_0 of the transverse point excitation are in the ranges of [16.62kN, 20.70kN], [20.64kN, 21.96kN] and [28.56kN, 30kN].

4.3 Comparisons of Parametrically Excited Vibrations

When the transverse point excitation is $F_0 = 1000\,\mathrm{N}$ and subjects to the point $(\zeta_0, \xi_0) = (1/3, 1/3)$, in order to illustrate the effect of the GPL weight fraction on the parametrically excited nonlinear vibrations of the GRC plates, Figures 9-14 demonstrate the occurrence of the chaotic vibrations for the prestressed U GRC plates with different GPL weight fractions. Both the in-plane uniaxial and biaxial excitations are considered in this subsection. Here, $g_G = 0.00\%$ represents the pure epoxy plate.

Under the in-plane uniaxial excitation $q_x(x, y, z) = q_{x0}\cos(\Omega_1 t)$, Figures 9(a)-9(d) indicate the bifurcation diagrams of the first four vibration modes for the prestressed U GRC plates with different GPL weight fractions $g_G = 0.00\%$, 0.25% and 0.50%, respectively. As the amplitudes of the in-plane uniaxial excitations q_{x0} increase from 0 to

2×10^8 N/m^2, the vibration laws of the prestressed U GRC plates with different GPL weight fractions are same, namely, the periodic $\rightarrow$ multi-periodic $\rightarrow$ short-time chaotic $\rightarrow$ multi-periodic $\rightarrow$ chaotic vibrations. Nevertheless, the chaotic vibrations are excited by using different uniaxial excitations q_{x0} for the prestressed U GRC plates with different GPL weight fractions. The chaotic vibrations happen firstly in the prestressed U GRC plate with $g_G = 0.00\%$, then with $g_G = 0.25\%$ and lastly with $g_G = 0.50\%$. It is illustrated that the GPL reinforcements can postpone the appearance of the chaotic vibrations in the prestressed GRC plate.

Figures 10 and 11 respectively reveal the nonlinear vibration properties of the first four vibration modes for the prestressed U GRC plates with different GPL weight fractions $g_G = 0.00\%$ and $g_G = 0.25\%$ when $q_{x0} = 5.96\times10^7$ N/m^2. As seen in Figure 10, the prestressed U GRC plates with the GPL weight fraction $g_G = 0.00\%$, namely pure epoxy plate, the chaotic vibrations occur. For the prestressed U GRC plate with $g_G = 0.25\%$, Figure 11 shows the 2-periodic motion. It is proved that even a small amount of GPL reinforcements can stabilize the vibration stability of the typical prestressed epoxy plate.

Setting $q_{x0} = q_{y0} = q_0$, Figure 12 gives the bifurcation phenomena of the first-order, second-order and forth-order vibration modes for the prestressed U GRC plates under the in-plane biaxial excitation with different GPL weight fractions, namely, $g_G = 0.00\%$, 0.25% and 0.50%. As the in-plane biaxial excitation q_0 increases from 0 to 1.2×10^8 N/m^2, three chaotic vibration ranges exist for the prestressed pure plate, but there is only one chaotic vibration range for the prestressed U GRC plates with the GPL weight fractions $g_G = 0.25\%$ and $g_G = 0.50\%$. The in-plane biaxial excitations q_0 are respectively [2.58, 2.89] $\times10^7$ N/m^2, [3.83, 3.98] $\times10^7$ N/m^2 and [7.85, 10.14] $\times10^7$ N/m^2 for the prestressed pure plate, [8.52, 9.82] $\times10^7$ N/m^2 for the prestressed U GRC plate with the GPL weight fraction $g_G = 0.25\%$ and [11.63, 12.00] $\times10^7$ N/m^2 for the prestressed U GRC plate with the GPL weight fraction $g_G = 0.50\%$.

Figures 13 and 14 respectively demonstrate the nonlinear vibration characteristics of the prestressed U GRC plate with GPL weight fraction $g_G = 0.25\%$ and 0.50% when in-plane biaxial excitation is $q_0 = 9.12\times10^7$ N/m^2. It is found that the prestressed U GRC plate with $g_G = 0.25\%$ has the chaotic vibrations, but the prestressed U GRC plate with $g_G = 0.50\%$ vibrates periodically. It implies that the increasing GPL weight fraction can

enhance the vibration stability of the prestressed U GRC plate.

5. Conclusions

This paper compares the natural frequencies and nonlinear vibrations among the pure polymer plate and GRC plates under combined the transverse and axial loads. All the edges of the plates are supposed to be the simply supported. Three distribution forms of the GPL reinforcements are considered, including the uniform pattern and FG patterns. The governing equations of motion for the pure polymer plate and GRC plates are derived based on the first-order shear deformation plate theory, von Kármán nonlinear geometric relationship and Hamilton's principle. The resulting equations are then discretized by the fourth-order Galerkin truncation. The first four order dimensionless natural frequencies of the pure polymer plate and GRC plates with different geometric characteristics are respectively checked. The time-histories, phase portraits and Poincaré maps of the prestressed pure polymer and GRC plates are examined under various transverse excitations and in-plane excitations. The effects of different distribution forms and weight fractions of the GPLs on the chaotic vibration regions and nonlinear vibration amplitudes of the prestressed GRC plates are also discussed in detailed. The major research findings of this work are summarized.

(1) With the increasing length of the square polymer composite plates, the first four order natural frequencies in the plates decrease. However, the first four order dimensionless frequencies can be significantly improved by the reinforcement of the GPLs.

(2) The GPLs can postpone the appearance of the chaotic vibrations for the typical prestressed polymer composite plates. The FG-X GRC plate is the best pattern to resist against the occurrence of the chaotic vibrations.

(3) The GPLs can reduce the nonlinear vibration amplitudes of the typical prestressed polymer composite plates and the nonlinear vibration properties of the prestressed GRC plates can be further strengthened by the increasing GPL weight fraction.

(4) The eccentric transverse point excitation and in-plane biaxial excitations are prone to induce the nonlinear vibration instability for the prestressed pure polymer and GRC plates.

Acknowledgements

The authors gratefully acknowledge the support of National Natural Science Foundation of China (NNSFC) through Grant Nos. 11802005, 11832002 and 11427801, the Funding Project for Academic Human Resources Development in Institutions of Higher Learning under the Jurisdiction of Beijing Municipality (PHRIHLB). The Research Impact Fund (Project No. R-5020-18) from the Research Grants Council of the Hong Kong Special Administrative Region is also acknowledged.

Conflict of Interest Statement

The authors declare that there is no conflict of interests regarding the publication of this paper.

Reference

1. G. Mittal, V. Dhand, K. Y. Rhee, S. J. Park and W. R. Lee, A review on carbon nanotubes and graphene as fillers in reinforced polymer nanocomposites, Journal of Industrial and Engineering Chemistry 21, p11-25, 2015.
2. K. M. Liew, Z. X. Lei and L. W. Zhang, Mechanical analysis of functionally graded carbon nanotube reinforced composites: a review, Composite Structures 120, p90-97, 2015.
3. K. M. Liew, Z. Z. Pan and L. W. Zhang, The recent progress of functionally graded CNT reinforced composites and structures, Science China Physics, Mechanics and Astronomy 63, 234601, 2020.
4. F. H. Gojny, M. H. G. Wichmann, B. Fiedler and K. Schulte, Influence of different carbon nanotubes on the mechanical properties of epoxy matrix composites - A comparative study, Composites Science and Technology 65, p2300-2313, 2005.
5. E. W. Wong, P. E. Sheehan and C. M. Lieber, Nanobeam mechanics: Elasticity, strength, and toughness of nanorods and nanotubes, Science 277, p1971-1975, 1997.
6. M. A. Rafiee, J. Rafiee, Z. Wang, H. Song, Z. Z. Yu and N. Koratkar, Enhanced mechanical properties of nanocomposites at low graphene content, ACS nano 3, p3884-3890, 2009.

7. C. Feng, S. Kitipornchai and J. Yang, Nonlinear free vibration of functionally graded polymer composite beams reinforced with graphene nanoplatelets (GPLs), Engineering Structures 140, p110-119, 2017.
8. T. K. Das and S. Prusty, Graphene-based polymer composites and their applications, Polymer-Plastics Technology and Engineering 52, p319-331, 2013.
9. C. H. Sun, F. Li, H. M. Cheng and G. Q. Lu, Axial Young's modulus prediction of single-walled carbon nanotube arrays with diameters from nanometer to meter scales, Applied Physics Letters 87, 2005.
10. J. F. Wang and W. Zhang, An equivalent continuum meshless approach for material nonlinear analysis of CNT-reinforced composites, Composite Structures 188, p116-125, 2018.
11. X. Y. Guo and W. Zhang, Nonlinear vibrations of a reinforced composite plate with carbon nanotubes, Composite Structures 135, p96-108, 2016.
12. S. Suresh and A. Mortensen, Fundamentals of functionally graded materials, The Institut of Materials, 1998.
13. J. Liu, L. L. Ke, Y. S. Wang, J. Yang and F. Alam, Thermoelastic frictional contact of functionally graded materials with arbitrarily varying properties, International Journal of Mechanical Sciences 63, p86-98, 2012.
14. H. S. Shen, Nonlinear bending of functionally graded carbon nanotube-reinforced composite plates in thermal environments, Composite Structures 91, p9-19, 2009.
15. Z. X. Wang and H. S. Shen, Nonlinear dynamic response of nanotube-reinforced composite plates resting on elastic foundations in thermal environments, Nonlinear Dynamics 70, p735-754, 2012.
16. Y. Q. Wang and J. W. Zu, Vibration behaviors of functionally graded rectangular plates with porosities and moving in thermal environment, Aerospace Science and Technology 69, p550-562, 2017.
17. Y. Q. Wang, Electro-mechanical vibration analysis of functionally graded piezoelectric porous plates in the translation state, Acta Astronautica 143, p263-271, 2018.
18. Y. Q. Wang and J. W. Zu, Nonlinear steady-state responses of longitudinally traveling functionally graded material plates in contact with liquid, Composite Structures 164, p130-144, 2017.
19. W. Zhang, J. Yang and Y. X. Hao, Chaotic vibrations of an orthotropic FGM rectangular plate based on third-order shear deformation theory, Nonlinear Dynamics

59, p619-660, 2010.

20. Y. X. Hao, L. H. Chen, W. Zhang and J. G. Lei, Nonlinear oscillations, bifurcations and chaos of functionally graded materials plate, Journal of Sound and Vibration 312, p862-892, 2008.
21. Y. Z. Liu, Y. X. Hao, W. Zhang, J. Chen and S. B. Li, Nonlinear dynamics of initially imperfect functionally graded circular cylindrical shell under complex loads, Journal of Sound and Vibration 348, p294-328, 2015.
22. S. W. Yang, Y. X. Hao, W. Zhang and S. B. Li, Nonlinear Dynamic Behavior of Functionally Graded Truncated Conical Shell Under Complex Loads, International Journal of Bifurcation and Chaos 25, 2015.
23. F. Liang, X. D. Yang, R. D. Bao and W. Zhang, Frequency Analysis of Functionally Graded Curved Pipes Conveying Fluid, Advances in Materials Science and Engineering 2016.
24. D. X. Cao, Y. H. Gao, M. H. Yao and W. Zhang, Free vibration of axially functionally graded beams using the asymptotic development method, Engineering Structures 173, p442-448, 2018.
25. L.W. Zhang, K. M. Liew and J. N. Reddy, Postbuckling behavior of bi-axially compressed arbitrarily straight-sided quadrilateral functionally graded material plates. Computer Methods in Applied Mechanics and Engineering 300, p593-610, 2016.
26. L.W. Zhang, K. M. Liew and J. N. Reddy, Postbuckling analysis of bi-axially compressed laminated nanocomposite plates using the first-order shear deformation theory, Composite Structures 152, p418-431, 2016.
27. L. L. Ke, J. Yang and S. Kitipornchai, Nonlinear free vibration of functionally graded carbon nanotube-reinforced composite beams, Composite Structures 92, p676-683, 2010.
28. L. L. Ke, J. Yang and S. Kitipornchai, Dynamic stability of functionally graded carbon nanotube-reinforced composite beams, Mechanics of Advanced Materials and Structures 20, p28-37, 2013.
29. Z. X. Lei, B. B. Yin and K. M. Liew, Bending and vibration behaviors of matrix cracked hybrid laminated plates containing CNTR-FG layers and FRC layers, Composite Structures 184, p314-326, 2018.
30. Z. Z. Pan, L. W. Zhang and K. M. Liew. Modeling geometrically nonlinear large deformation behaviors of matrix cracked hybrid composite deep shells containing CNTRC layers. Computer Methods in Applied Mechanics and Engineering 355,

p753-778, 2019.

31. Z. Z. Pan and K. M. Liew. Predicting vibration characteristics of rotating composite blades containing CNT-reinforced composite laminae and damaged fiber-reinforced composite laminae. Composite Structures 250, 112580, 2020.
32. L. W. Zhang, Z. X. Lei and K. M. Liew, Free vibration analysis of FG-CNT reinforced composite straight-sided quadrilateral plates resting on elastic foundations using the IMLS-Ritz method, Journal of Vibration and Control 23, p1026-1043, 2017.
33. L. W. Zhang, On the study of the effect of in-plane forces on the frequency parameters of CNT-reinforced composite skew plates, Composite Structures 160, p824-837, 2017.
34. L. W. Zhang, and B. A. Selim. Vibration analysis of CNT-reinforced thick laminated composite plates based on Reddy's higher-order shear deformation theory, Composite Structures 160, p689-705, 2017.
35. L. W. Zhang, Z. G. Song, and K. M. Liew, Computation of aerothermoelastic properties and active flutter control of CNT reinforced functionally graded composite panels in supersonic airflow, Computer Methods in Applied Mechanics and Engineering 300, p427-441, 2016.
36. L. W. Zhang, Z. G. Song, P. Qiao and K. M. Liew, Modeling of dynamic responses of CNT-reinforced composite cylindrical shells under impact loads. Computer Methods in Applied Mechanics and Engineering 313, p889-903, 2017.
37. K. S. Novoselov, A. K. Geim, S. V. Morozov, D. Jiang, Y. Zhang, S. V. Dubonos, I. V. Grigorieva and A. A. Firsov, Electric field effect in atomically thin carbon films, Science 306, p666-669, 2004.
38. X. Zhao, Q. Zhang, D. Chen and P. Lu, Enhanced mechanical properties of graphene-based poly (vinyl alcohol) composites, Macromolecules 43, p2357-2363, 2010.
39. D. X. Luong, K. V. Bets, W. A. Algozeeb, M. G. Stanford, C. Kittrell, W. Chen, R. V. Salvatierra, M. Ren, E. A. McHugh and P. A. Advincula, Gram-scale bottom-up flash graphene synthesis, Nature 577, p647-651, 2020.
40. Y. Zhang, K. M. Liew and D. Hui, Characterizing nonlinear vibration behavior of bilayer graphene thin films, Composites Part B: Engineering 145, p197-205, 2018.
41. Y. Zhang, Z. X. Lei, L. W. Zhang, K. M. Liew and J. L. Yu, Nonlocal continuum model for vibration of single-layered graphene sheets based on the element-free kp-Ritz method, Engineering Analysis with Boundary Elements 56, p90-97, 2015.

42. J. Yan, S. Lai and L. He, Nonlinear dynamic behavior of single-layer graphene under uniformly distributed loads, Composites Part B: Engineering 2019.
43. X. Y. Guo, P. Jiang, W. Zhang, J. Yang, S. Kitipornchai and L. Sun, Nonlinear dynamic analysis of composite piezoelectric plates with graphene skin, Composite Structures 206, p839-852, 2018.
44. S. Y. Zhao, Z. Zhao, Z. C. Yang, L. L. Ke, S. Kitipornchai and J. Yang, Functionally graded graphene reinforced composite structures: A review, Engineering Structures 210, p110339, 2020.
45. M. T. Song, S. Kitipornchai and J. Yang, Free and forced vibrations of functionally graded polymer composite plates reinforced with graphene nanoplatelets, Composite Structures 159, p579-588, 2017.
46. B. Yang, J. Mei, D. Chen, F. Yu and J. Yang, 3D thermo-mechanical solution of transversely isotropic and functionally graded graphene reinforced elliptical plates, Composite Structures 184, p1040-1048, 2018.
47. X. Q. Li, M. T. Song, J. Yang and S. Kitipornchai, Primary and secondary resonances of functionally graded graphene platelet-reinforced nanocomposite beams, Nonlinear Dynamics 2018.
48. H. S. Shen, Y. Xian, Y. Fan and D. Hui, Nonlinear vibration of functionally graded graphene-reinforced composite laminated cylindrical panels resting on elastic foundations in thermal environments, Composites Part B-Engineering 136, p177-186, 2018.
49. F. Ebrahimi, M. Nouraei and A. Dabbagh, Modeling vibration behavior of embedded graphene-oxide powder-reinforced nanocomposite plates in thermal environment, Mechanics Based Design of Structures and Machines p1-24, 2019.
50. J. J. Mao and W. Zhang, Linear and nonlinear free and forced vibrations of graphene reinforced piezoelectric composite plate under external voltage excitation, Composite Structures 203, p551-565, 2018.
51. J. J. Mao, H. M. Lu, W. Zhang and S. K. Lai, Vibrations of graphene nanoplatelet reinforced functionally gradient piezoelectric composite microplate based on nonlocal theory, Composite Structures 236, 2020.
52. A. W. Wang, H. Y. Chen, Y. X. Hao and W. Zhang, Vibration and bending behavior of functionally graded nanocomposite doubly-curved shallow shells reinforced by graphene nanoplatelets, Results in Physics 9, p550-559, 2018.
53. A. Nosier and J. Reddy, A study of non-linear dynamic equations of higher-order

shear deformation plate theories, International Journal of Non-Linear Mechanics 26, p233-249, 1991.

54. G. Yao and Y. M. Zhang, Dynamics and stability of an axially moving plate interacting with surrounding airflow, Meccanica 51, p2111-2119, 2016.

Appendix A

The dimensionless nonlinear terms $\overline{Z}_1$ and $\overline{Z}_2$ in equation (20) are expressed as

$$\begin{aligned}\overline{Z}_1 = &\left[\overline{A}_{11}\left(\frac{1}{\eta}\frac{\partial^2 u}{\partial\zeta^2}+\frac{1}{\eta^2}\frac{\partial w}{\partial\zeta}\frac{\partial^2 w}{\partial\zeta^2}\right)+\overline{A}_{12}\left(\frac{\lambda}{\eta}\frac{\partial^2 v}{\partial\zeta\partial\xi}+\frac{\lambda^2}{\eta^2}\frac{\partial w}{\partial\xi}\frac{\partial^2 w}{\partial\zeta\partial\xi}\right)\right]\frac{\partial w}{\partial\zeta}\\ &+\left\{\overline{A}_{11}\left[\frac{1}{\eta}\frac{\partial u}{\partial\zeta}+\frac{1}{2\eta^2}\left(\frac{\partial w}{\partial\zeta}\right)^2\right]+\overline{A}_{12}\left[\frac{\lambda}{\eta}\frac{\partial v}{\partial\xi}+\frac{\lambda^2}{2\eta^2}\left(\frac{\partial w}{\partial\xi}\right)^2\right]\right\}\frac{\partial^2 w}{\partial\zeta^2}\\ &+\left[\overline{A}_{12}\left(\frac{\lambda}{\eta}\frac{\partial^2 u}{\partial\zeta\partial\xi}+\frac{\lambda}{\eta^2}\frac{\partial w}{\partial\zeta}\frac{\partial^2 w}{\partial\zeta\partial\xi}\right)+\overline{A}_{22}\left(\frac{\lambda^2}{\eta}\frac{\partial^2 u}{\partial\xi^2}+\frac{\lambda^3}{\eta^2}\frac{\partial w}{\partial\xi}\frac{\partial^2 w}{\partial\xi^2}\right)\right]\lambda\frac{\partial w}{\partial\xi}\\ &+\left\{\overline{A}_{12}\left[\frac{1}{\eta}\frac{\partial u}{\partial\zeta}+\frac{1}{2\eta^2}\left(\frac{\partial w}{\partial\zeta}\right)^2\right]+\overline{A}_{22}\left[\frac{\lambda}{\eta}\frac{\partial v}{\partial\xi}+\frac{\lambda^2}{2\eta^2}\left(\frac{\partial w}{\partial\xi}\right)^2\right]\right\}\lambda^2\frac{\partial^2 w}{\partial\xi^2},\end{aligned}\tag{A1}$$

$$\begin{aligned}\overline{Z}_2 = &\overline{A}_{66}\left(\frac{\lambda}{\eta}\frac{\partial^2 u}{\partial\zeta\partial\xi}+\frac{1}{\eta}\frac{\partial^2 v}{\partial\zeta^2}+\frac{\lambda}{\eta^2}\frac{\partial w}{\partial\xi}\frac{\partial^2 w}{\partial\zeta^2}+\frac{\lambda}{\eta^2}\frac{\partial w}{\partial\zeta}\frac{\partial^2 w}{\partial\zeta\partial\xi}\right)\lambda\frac{\partial w}{\partial\xi}\\ &+\overline{A}_{66}\left(\frac{\lambda^2}{\eta}\frac{\partial^2 u}{\partial\xi^2}+\frac{\lambda}{\eta}\frac{\partial^2 v}{\partial\zeta\partial\xi}+\frac{\lambda^2}{\eta^2}\frac{\partial w}{\partial\xi}\frac{\partial^2 w}{\partial\zeta\partial\xi}+\frac{\lambda^2}{\eta^2}\frac{\partial w}{\partial\zeta}\frac{\partial^2 w}{\partial\xi^2}\right)\frac{\partial w}{\partial\zeta}\\ &+2\overline{A}_{66}\left(\frac{\lambda}{\eta}\frac{\partial u}{\partial\xi}+\frac{1}{\eta}\frac{\partial v}{\partial\zeta}+\frac{\lambda}{\eta^2}\frac{\partial w}{\partial\zeta}\frac{\partial w}{\partial\xi}\right)\lambda\frac{\partial^2 w}{\partial\zeta\partial\xi}.\end{aligned}\tag{A2}$$

Table captions

Table 1 First-order, second-order and forth-order dimensionless natural frequencies $\Omega h\sqrt{\rho_M / E_M}$ of the GRC plates with different GPL distribution patterns.

Table 2 Vibration amplitudes of the prestressed pure epoxy plate and GRC plates with different GPL distribution patterns and varying transverse point excitation.

Table 1

m, n	Pure epoxy		U Pattern		FG-O pattern		FG-X pattern	
	present	Ref. [45]	present	Ref. [45]	present	Ref. [45]	present	Ref. [45]
1,1	0.0589	0.0584	0.1225	0.1216	0.1028	0.1020	0.1388	0.1378
2,1	0.1428	0.1391	0.2940	0.2895	0.2497	0.2456	0.3297	0.3249
2,2	0.2177	0.2132	0.4531	0.4436	0.3888	0.3796	0.5034	0.4939
3,1	0.2658	0.2595	0.5319	0.5400	0.4776	0.4645	0.6114	0.5984
3,2	0.3342	0.3251	0.6956	0.6767	0.6055	0.5860	0.7633	0.7454

Table 2

		$F_0 = 10$ kN	$F_0 = 15$ kN	$F_0 = 20$ kN	$F_0 = 25$ kN
x_1	Pure	1.41	1.52	1.24	1.41
	U	0.78	0.87	0.90	0.94
	FG-X	0.70	0.78	0.83	0.67
	FG-O	0.85	0.91	0.96	1.00
x_3	Pure	0.21	0.20	0.12	0.12
	U	0.06	0.22	0.13	0.17
	FG-X	0.06	0.09	0.14	0.50
	FG-O	0.06	0.09	0.12	0.16
x_7	Pure	0.15	0.15	0.62	0.55
	U	0.02	0.04	0.05	0.06
	FG-X	0.02	0.03	0.04	0.06
	FG-O	0.04	0.06	0.08	0.10

Figure Captions

Figure 1 Schematic configuration of a *K*-layered prestressed GRC plate subjected to complex excitations (a) and GPL distribution patterns: U (b), FG-X (c) and FG-O (d).

Figure 2 Effects of the length on the first four dimensionless natural frequencies of the four type plates: pure epoxy (a), U (b), FG-X (c) and FG-O (d).

Figure 3 The bifurcation diagrams and two-dimensional phase portraits with Poincaré maps of the first-order vibration mode are given for the prestressed pure epoxy plate with $F_0 = 9000\,\mathrm{N}$ and varying dimensionless damping coefficient.

Figure 4 Bifurcation diagrams of the first-order mode for the prestressed pure epoxy plate (a) and GRC plates (b), second-order mode for pure epoxy plate (c) and GRC plates (d) and forth-order for pure epoxy plate (e) and GRC plates (f) under transverse point excitation.

Figure 5 Time histories and two-dimensional phase portraits with Poincaré maps of the first-order (τ, x_1) (a) and (x_1, x_2) (b), second-order (τ, x_2) (c) and (x_3, x_4) (d), and forth-order (τ, x_7) (e) and (x_7, x_8) (f) vibration modes for the prestressed pure epoxy plate when $F_0 = 9428\,\mathrm{N}$.

Figure 6 Time histories and two-dimensional phase portraits with Poincaré maps of the first-order (τ, x_1) (a) and (x_1, x_2) (b), second-order (τ, x_2) (c) and (x_3, x_4) (d), and forth-order (τ, x_7) (e) and (x_7, x_8) (f) vibration mode for the prestressed U GRC plate when $F_0 = 9428\,\mathrm{N}$.

Figure 7 Time histories, two-dimensional phase portraits with Poincaré maps and three-dimensional phase portraits: (τ, x_1) (a), (x_1, x_2) (c) and (x_1, x_2, x_3) (e) for the prestressed FG-X GRC plate and (τ, x_1) (b), (x_1, x_2) (d) and (x_1, x_2, x_3) (f) for the prestressed FG-O GRC plate when $F_0 = 9428\,\mathrm{N}$.

Figure 8 Bifurcation diagrams of four first-order vibration modes for the prestressed pure epoxy (a), U (b), FG-X (c) and FG-O (d) plates when the transverse point force subject to the different positions.

Figure 9 Bifurcation diagrams of the first-order (a), second-order (b), third-order (c) and forth-order (d) vibration modes for the prestressed U GRC plates with different GPL weight fraction.

Figure 10 Time histories and two-dimensional phase portraits with Poincaré maps of the first-order (τ, x_1) (a) and (x_1, x_2) (b), second-order (τ, x_2) (c) and (x_3, x_4) (d), third-order (τ, x_5) (e) and (x_5, x_6) (f), and forth-order (τ, x_7) (g) and (x_7, x_8) (h) vibration modes for the prestressed U GRC plate with $g_G = 0.00\%$ when $q_{x0} = 5.96 \times 10^7$ N/m^2.

Figure 11 Time histories and two-dimensional phase portraits with Poincaré maps of the first-order (τ, x_1) (a) and (x_1, x_2) (b), second-order (τ, x_2) (c) and (x_3, x_4) (d), third-order (τ, x_5) (e) and (x_5, x_6) (f), and forth-order (τ, x_7) (g) and (x_7, x_8) (h) vibration modes for the prestressed U GRC plate with $g_G = 0.25\%$ when $q_{x0} = 5.96 \times 10^7$ N/m^2.

Figure 12 Bifurcation diagrams of the first-order (a), second-order (b) and forth-order (c) vibration modes for the prestressed U GRC plates under in-plane biaxial excitation with different GPL weight fractions.

Figure 13 Time histories and two-dimensional phase portraits with Poincaré maps of the first-order (τ, x_1) (a) and (x_1, x_2) (b), second-order (τ, x_2) (c) and (x_3, x_4) (d), and forth-order (τ, x_7) (e) and (x_7, x_8) (f) vibration modes for the prestressed U GRC plate with $g_G = 0.25\%$ when $q_0 = 9.12 \times 10^7$ N/m^2.

Figure 14 Time histories and two-dimensional phase portraits with Poincaré maps of the first-order (τ, x_1) (a) and (x_1, x_2) (b), second-order (τ, x_2) (c) and (x_3, x_4) (d), and forth-order (τ, x_7) (e) and (x_7, x_8) (f) vibration modes for the prestressed U GRC plate with $g_G = 0.50\%$ when $q_0 = 9.12 \times 10^7$ N/m^2.

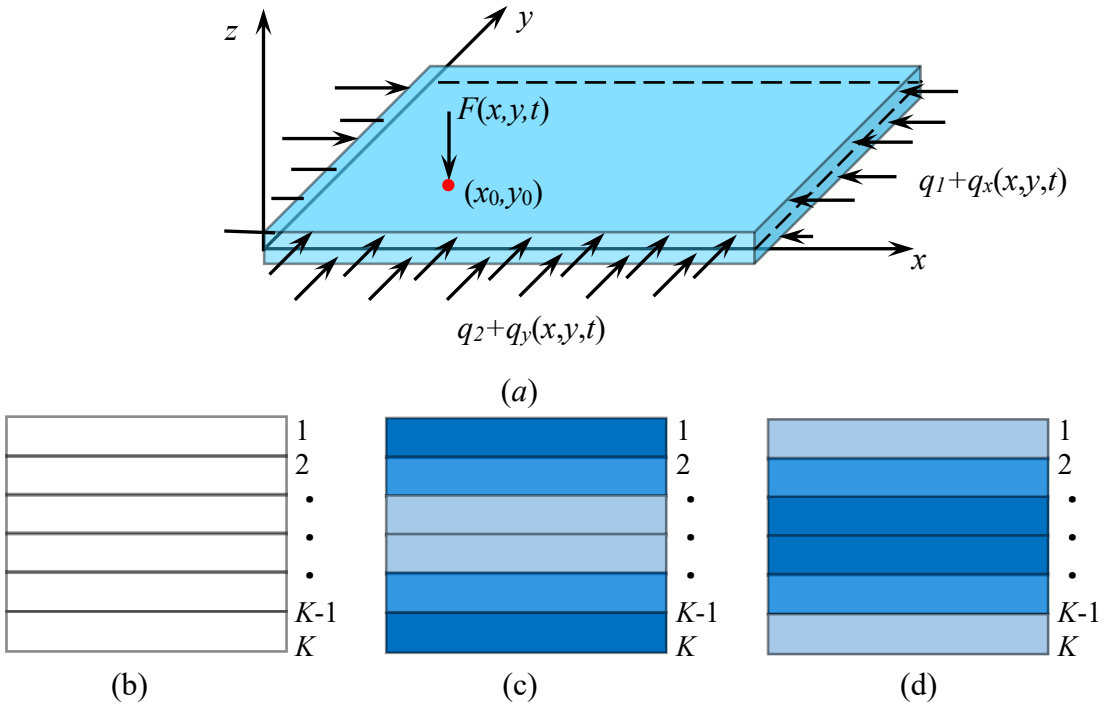

Figure 1

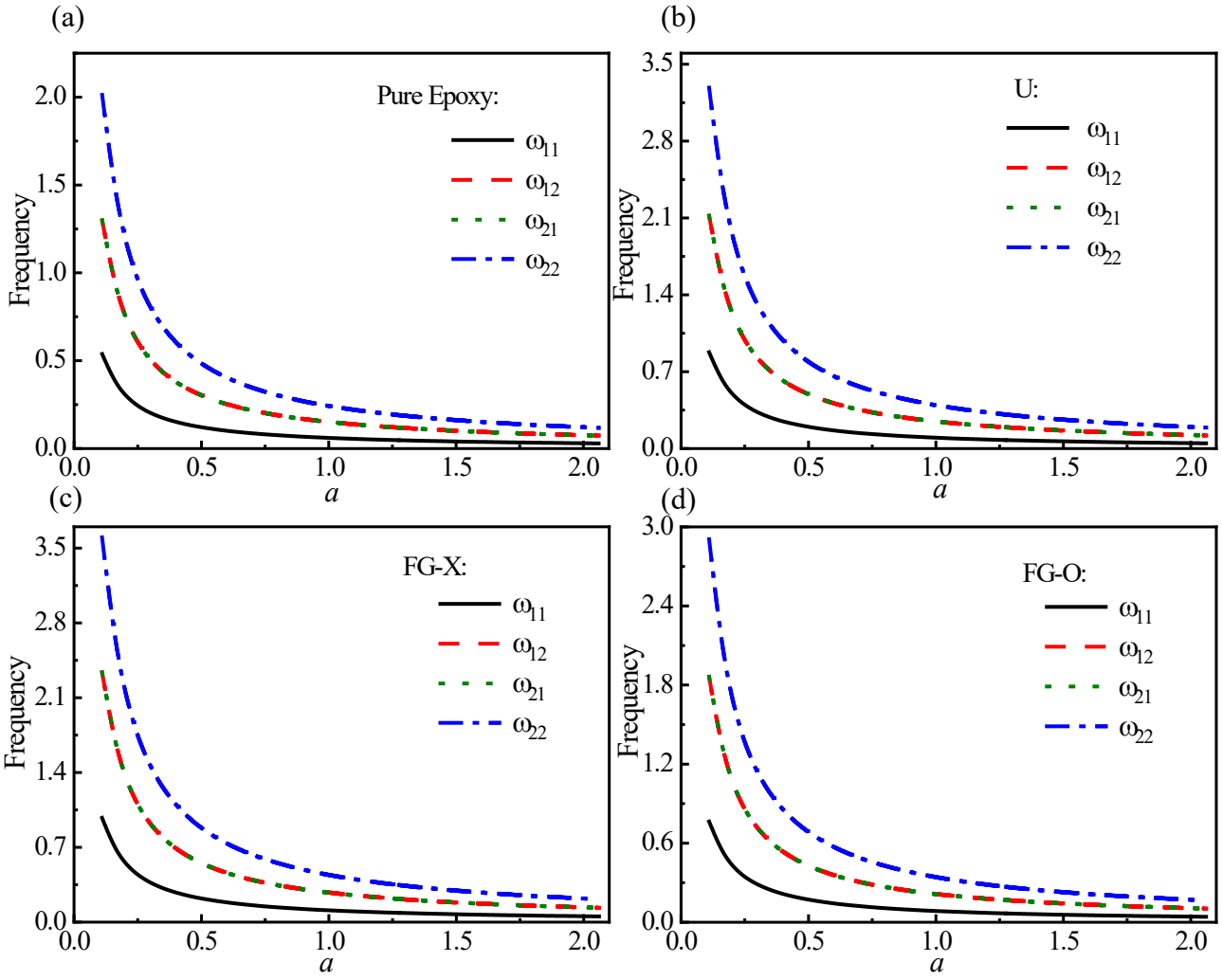

Figure 2

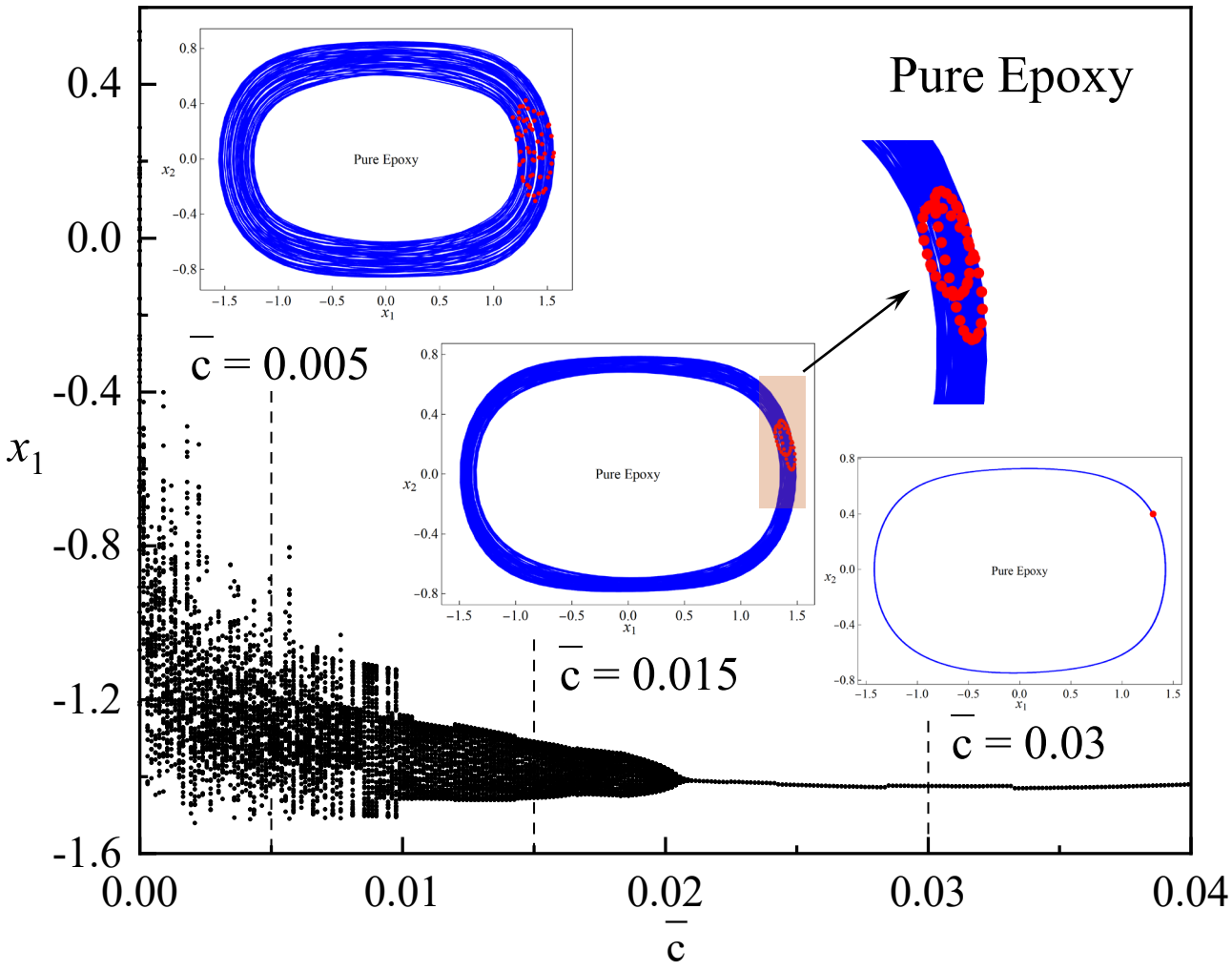
Pure Epoxy
$\overline{c} = 0.005$
$\overline{c} = 0.015$
$\overline{c} = 0.03$
x_1
$\overline{c}$
0.4
0.0
-0.4
-0.8
-1.2
-1.6
0.00
0.01
0.02
0.03
0.04

Figure 3

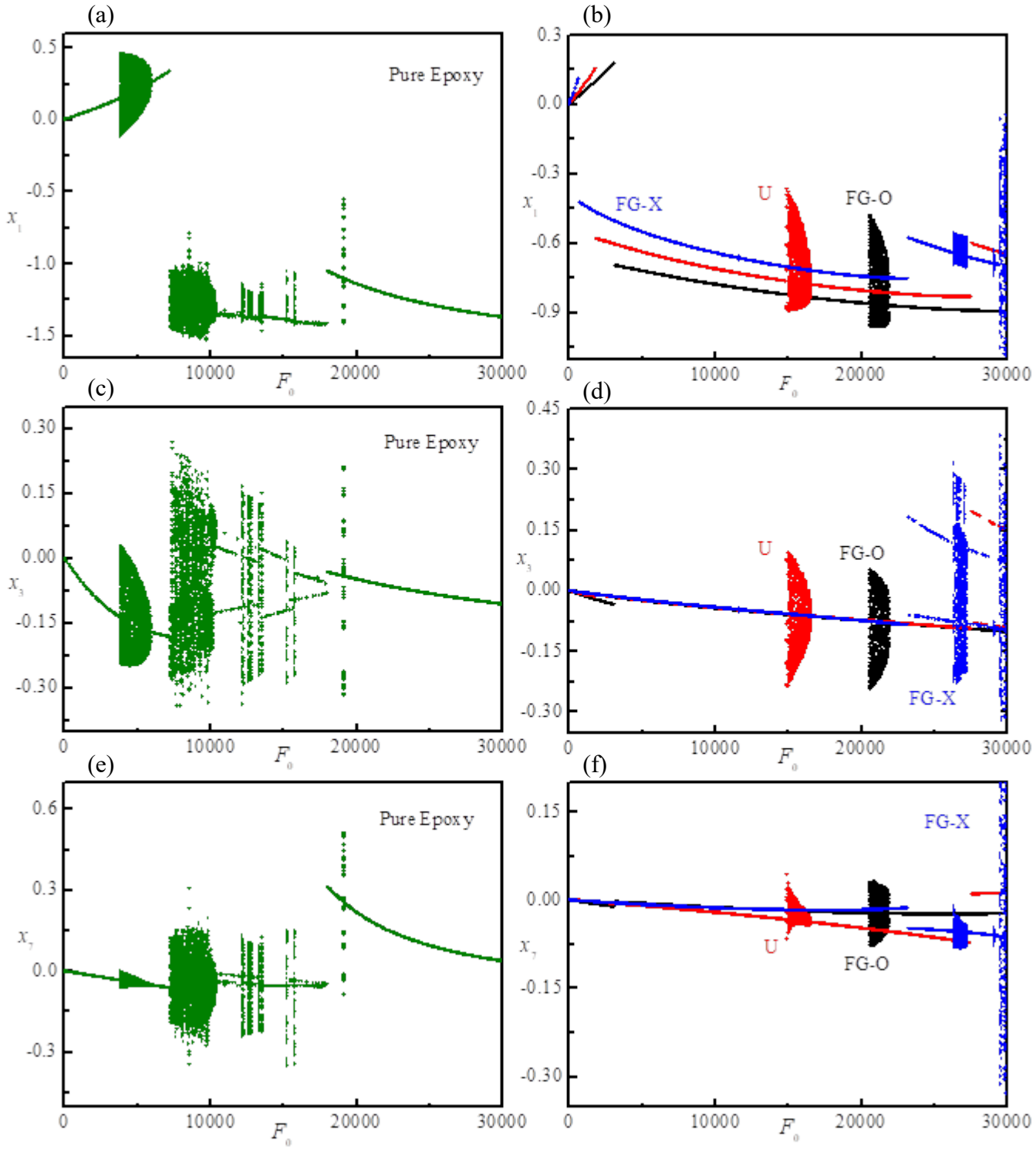
(a)
Pure Epoxy
(b)
FG-X
U
FG-O
(c)
Pure Epoxy
(d)
U
FG-O
FG-X
(e)
Pure Epoxy
(f)
FG-X
U
FG-O
F_0

Figure 4

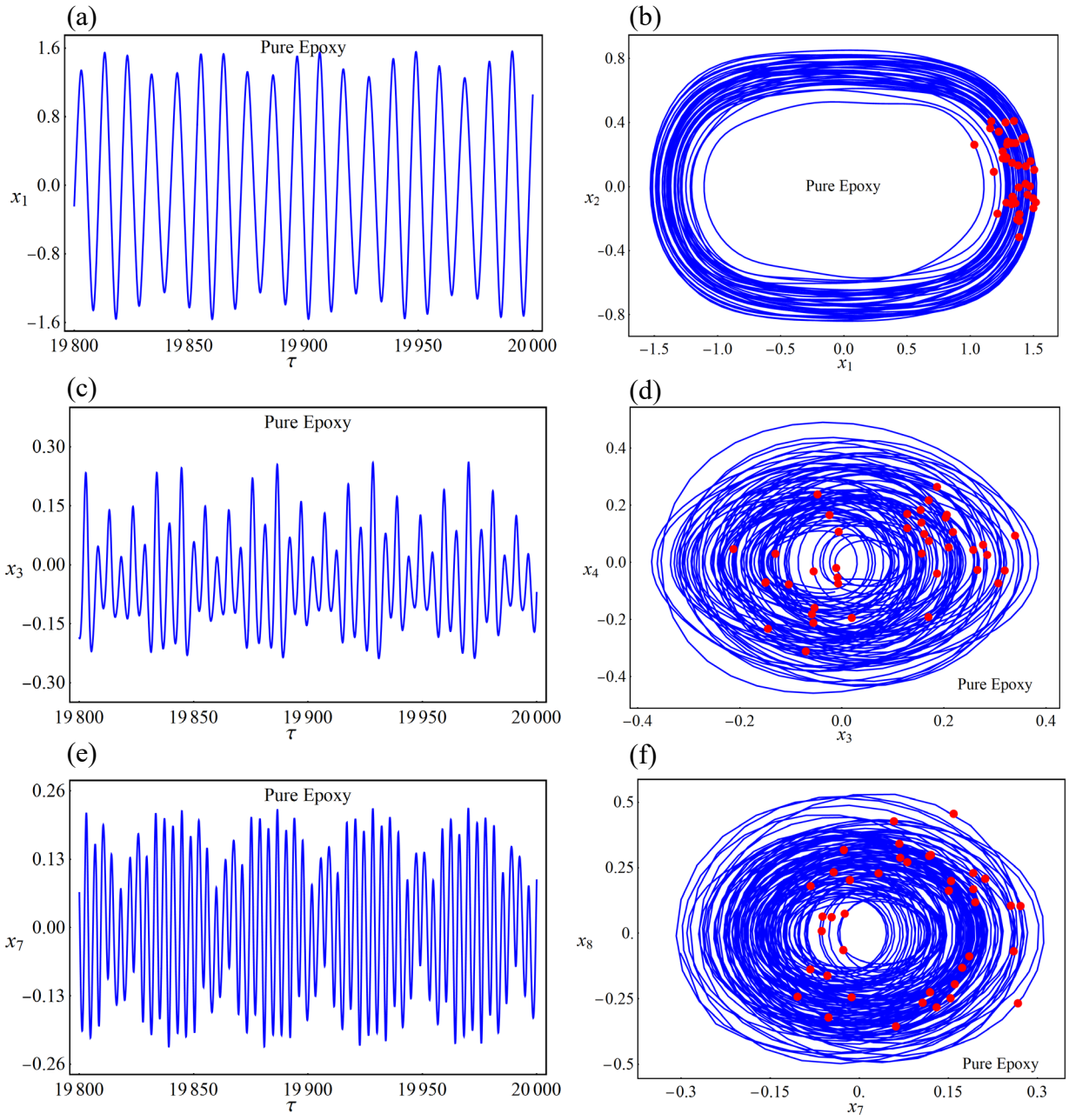
(a)
Pure Epoxy
1.6
0.8
0.0
−0.8
−1.6
x_1
19 800
19 850
19 900
19 950
20 000
τ
(b)
Pure Epoxy
0.8
0.4
0.0
−0.4
−0.8
x_2
−1.5
−1.0
−0.5
0.0
0.5
1.0
1.5
x_1
(c)
Pure Epoxy
0.30
0.15
0.00
−0.15
−0.30
x_3
19 800
19 850
19 900
19 950
20 000
τ
(d)
Pure Epoxy
0.4
0.2
0.0
−0.2
−0.4
x_4
−0.4
−0.2
0.0
0.2
0.4
x_3
(e)
Pure Epoxy
0.26
0.13
0.00
−0.13
−0.26
x_7
19 800
19 850
19 900
19 950
20 000
τ
(f)
Pure Epoxy
0.5
0.25
0.
−0.25
−0.5
x_8
−0.3
−0.15
0.
0.15
0.3
x_7

Figure 5

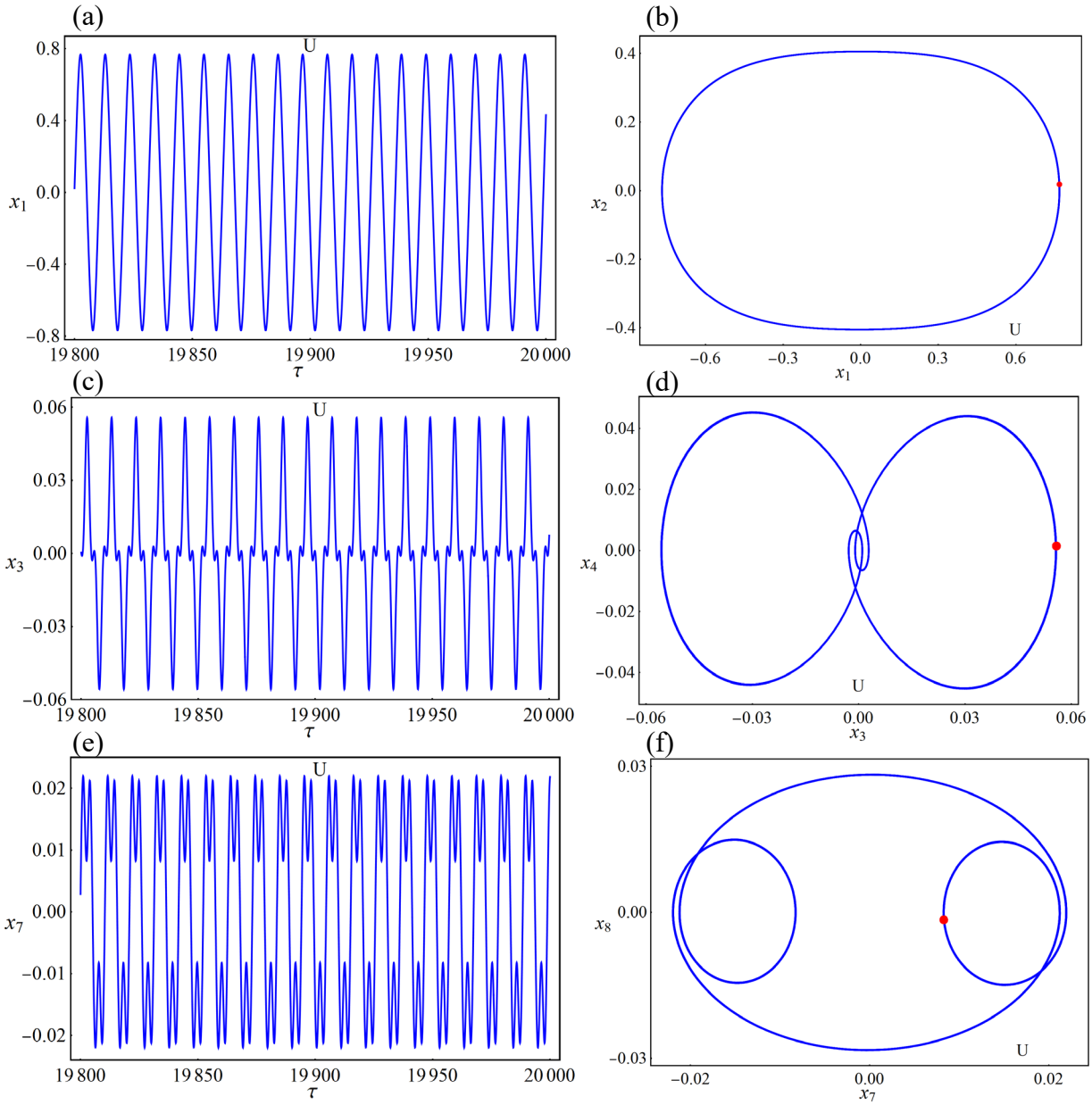
(a)
U
0.8
0.4
0.0
−0.4
−0.8
x_1
19 800
19 850
19 900
19 950
20 000
τ
(b)
0.4
0.2
0.0
−0.2
−0.4
x_2
U
−0.6
−0.3
0.0
0.3
0.6
x_1
(c)
U
0.06
0.03
0.00
−0.03
−0.06
x_3
19 800
19 850
19 900
19 950
20 000
τ
(d)
0.04
0.02
0.00
−0.02
−0.04
x_4
U
−0.06
−0.03
0.00
0.03
0.06
x_3
(e)
U
0.02
0.01
0.00
−0.01
−0.02
x_7
19 800
19 850
19 900
19 950
20 000
τ
(f)
0.03
0.00
−0.03
x_8
U
−0.02
0.00
0.02
x_7

Figure 6

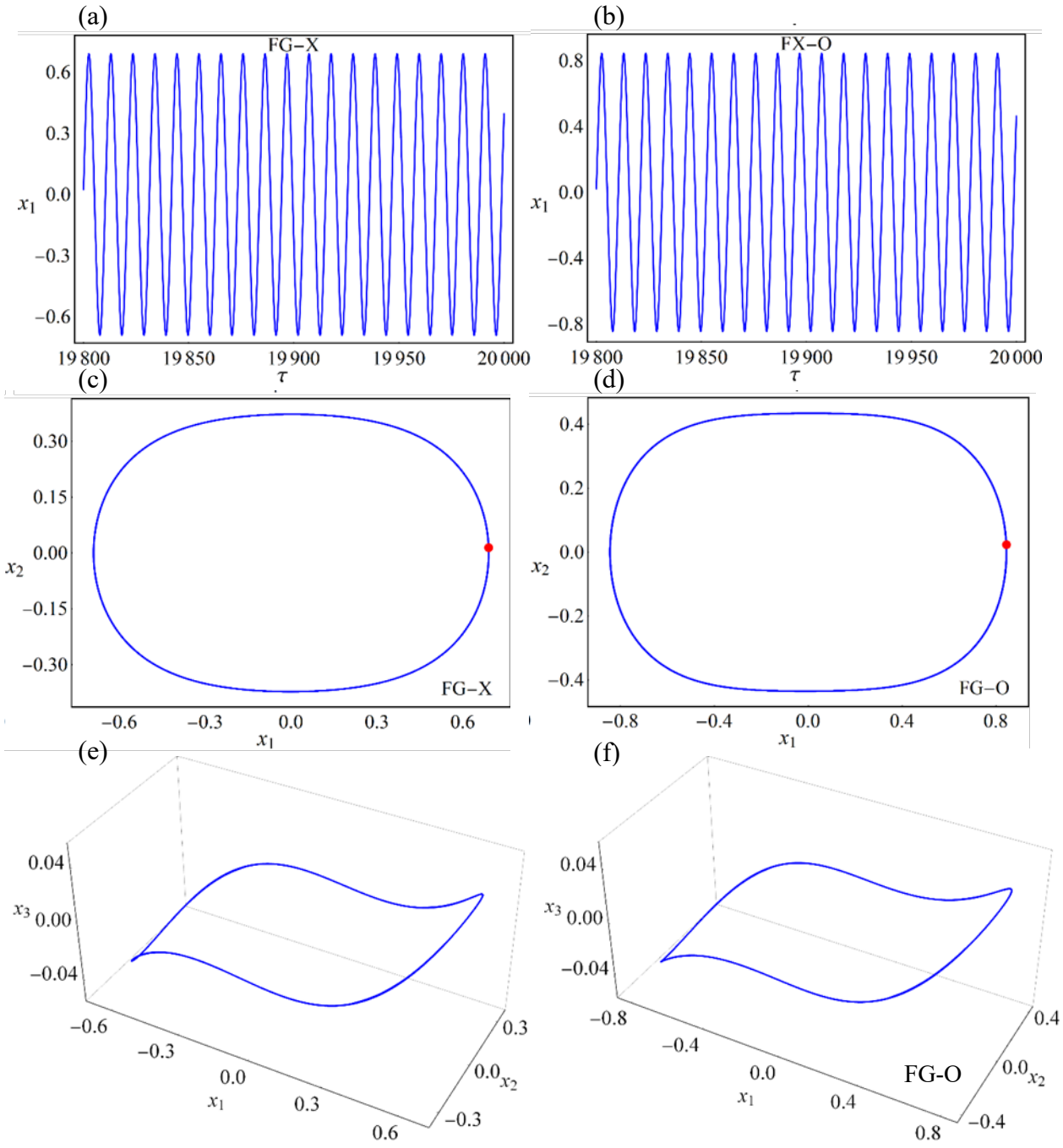
(a)
FG−X
0.6
0.3
0.0
−0.3
−0.6
x_1
19 800
19 850
19 900
19 950
20 000
τ
(b)
FX−O
0.8
0.4
0.0
−0.4
−0.8
x_1
19 800
19 850
19 900
19 950
20 000
τ
(c)
0.30
0.15
0.00
−0.15
−0.30
x_2
FG−X
−0.6
−0.3
0.0
0.3
0.6
x_1
(d)
0.4
0.2
0.0
−0.2
−0.4
x_2
FG−O
−0.8
−0.4
0.0
0.4
0.8
x_1
(e)
0.04
0.00
−0.04
x_3
−0.6
−0.3
0.0
0.3
0.6
x_1
0.3
0.0
−0.3
x_2
(f)
0.04
0.00
−0.04
x_3
−0.8
−0.4
0.0
0.4
0.8
x_1
FG-O
0.4
0.0
−0.4
x_2

Figure 7

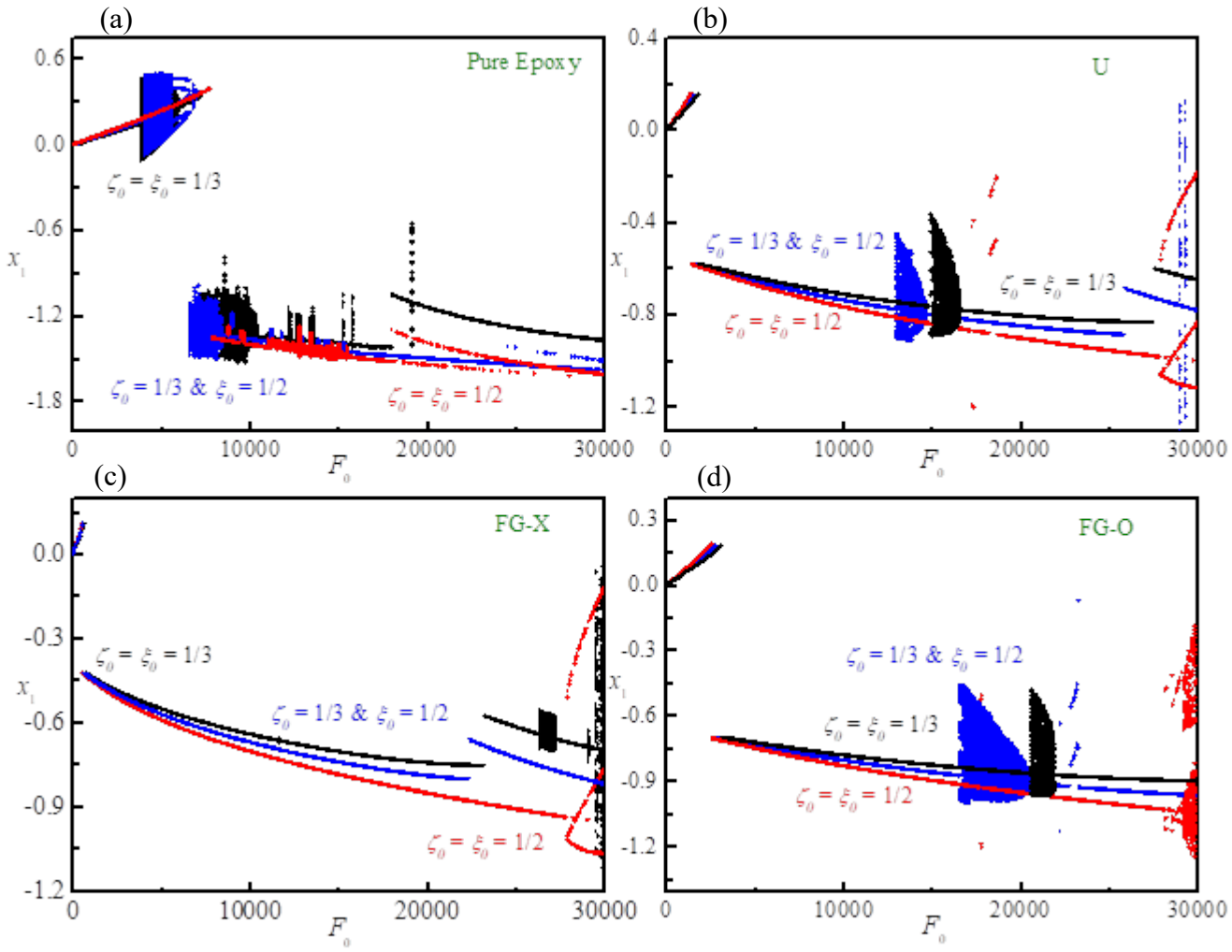
(a)
Pure Epoxy
$\zeta_0 = \xi_0 = 1/3$
$\zeta_0 = 1/3$ & $\xi_0 = 1/2$
$\zeta_0 = \xi_0 = 1/2$
(b)
U
$\zeta_0 = 1/3$ & $\xi_0 = 1/2$
$\zeta_0 = \xi_0 = 1/3$
$\zeta_0 = \xi_0 = 1/2$
(c)
FG-X
$\zeta_0 = \xi_0 = 1/3$
$\zeta_0 = 1/3$ & $\xi_0 = 1/2$
$\zeta_0 = \xi_0 = 1/2$
(d)
FG-O
$\zeta_0 = 1/3$ & $\xi_0 = 1/2$
$\zeta_0 = \xi_0 = 1/3$
$\zeta_0 = \xi_0 = 1/2$
X_1
F_0

Figure 8

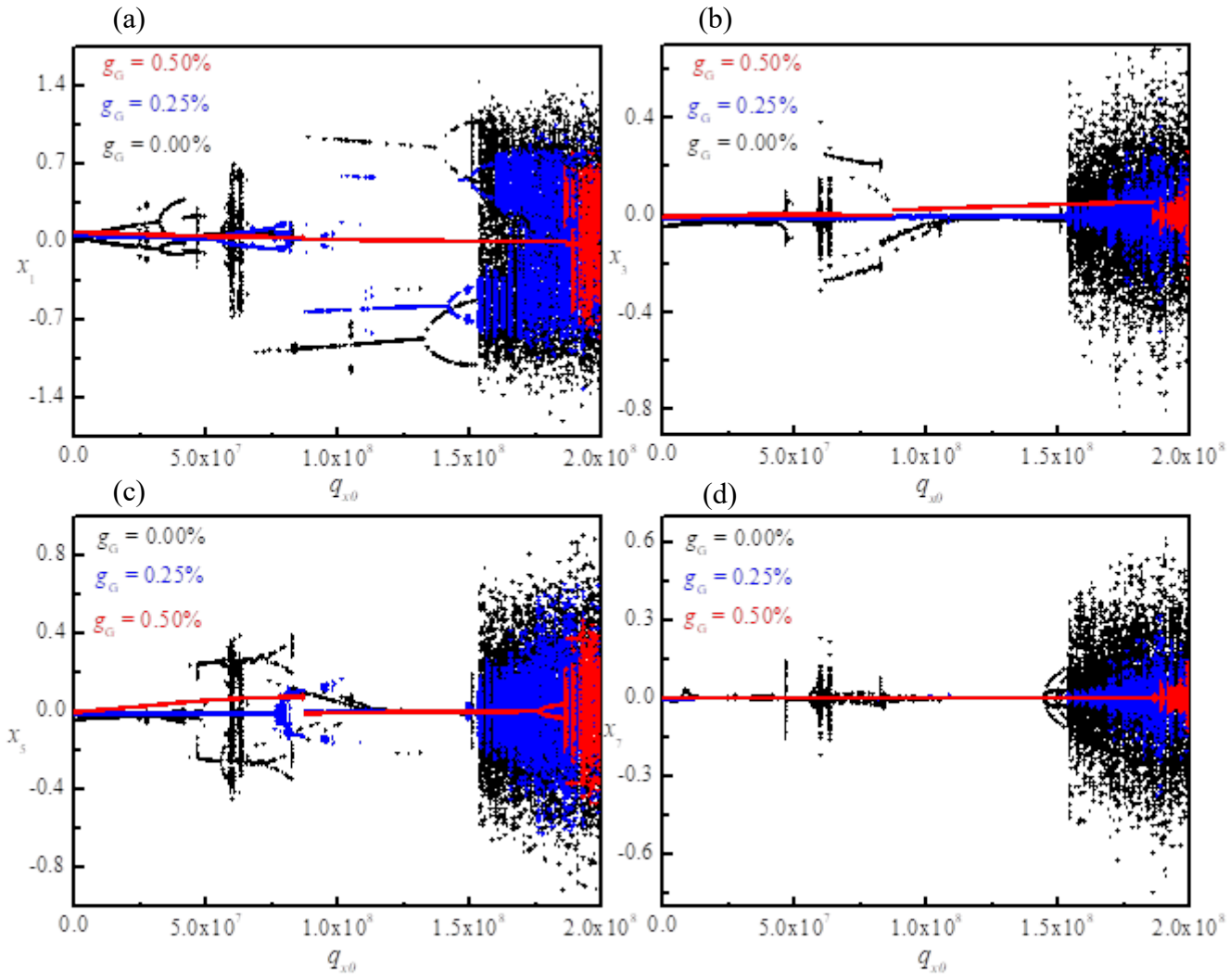
(a)
(b)
(c)
(d)
g_G = 0.50%
g_G = 0.25%
g_G = 0.00%
x_1
x_3
x_5
x_7
q_{x0}
0.0
5.0x10^7
1.0x10^8
1.5x10^8
2.0x10^8

Figure 9

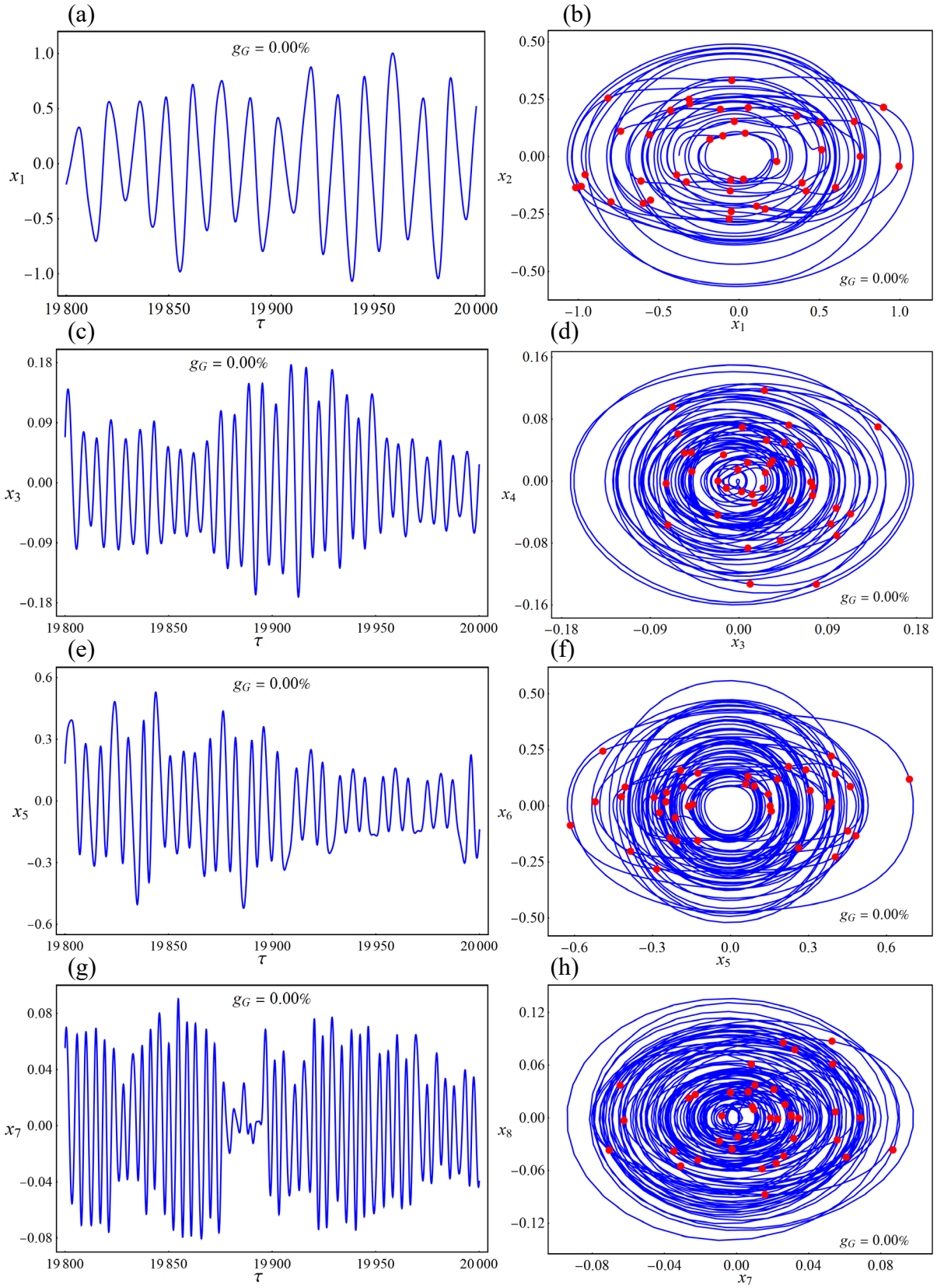
(a)
g_G = 0.00%
x_1
τ
(b)
g_G = 0.00%
x_2
x_1
(c)
g_G = 0.00%
x_3
τ
(d)
g_G = 0.00%
x_4
x_3
(e)
g_G = 0.00%
x_5
τ
(f)
g_G = 0.00%
x_6
x_5
(g)
g_G = 0.00%
x_7
τ
(h)
g_G = 0.00%
x_8
x_7

Figure 10

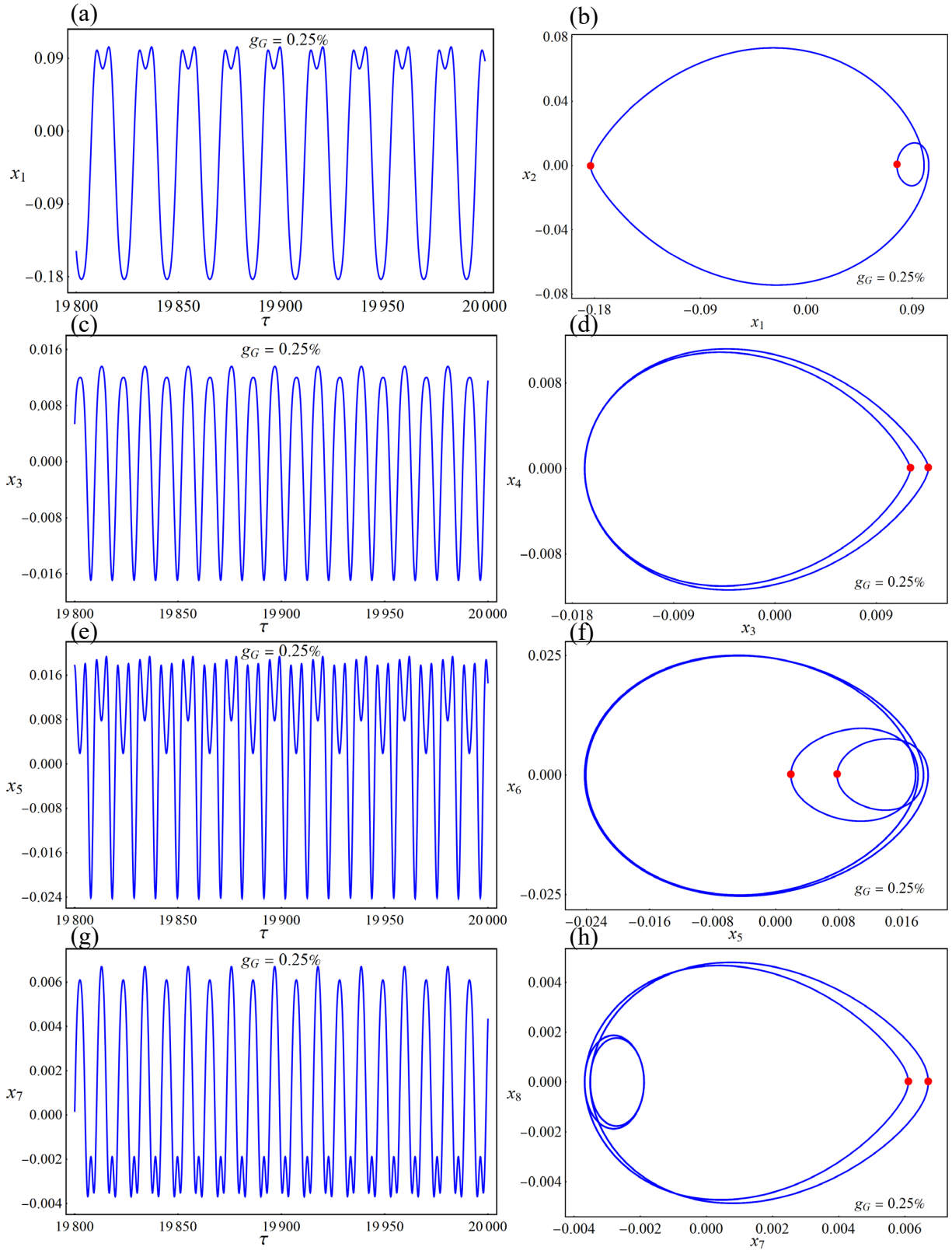
(a)
g_G = 0.25%
0.09
0.00
−0.09
−0.18
x_1
19 800
19 850
19 900
19 950
20 000
τ
(b)
0.08
0.04
0.00
−0.04
−0.08
x_2
g_G = 0.25%
−0.18
−0.09
0.00
0.09
x_1
(c)
g_G = 0.25%
0.016
0.008
0.000
−0.008
−0.016
x_3
19 800
19 850
19 900
19 950
20 000
τ
(d)
0.008
0.000
−0.008
x_4
g_G = 0.25%
−0.018
−0.009
0.000
0.009
x_3
(e)
g_G = 0.25%
0.016
0.008
0.000
−0.008
−0.016
−0.024
x_5
19 800
19 850
19 900
19 950
20 000
τ
(f)
0.025
0.000
−0.025
x_6
g_G = 0.25%
−0.024
−0.016
−0.008
0.000
0.008
0.016
x_5
(g)
g_G = 0.25%
0.006
0.004
0.002
0.000
−0.002
−0.004
x_7
19 800
19 850
19 900
19 950
20 000
τ
(h)
0.004
0.002
0.000
−0.002
−0.004
x_8
g_G = 0.25%
−0.004
−0.002
0.000
0.002
0.004
0.006
x_7

Figure 11

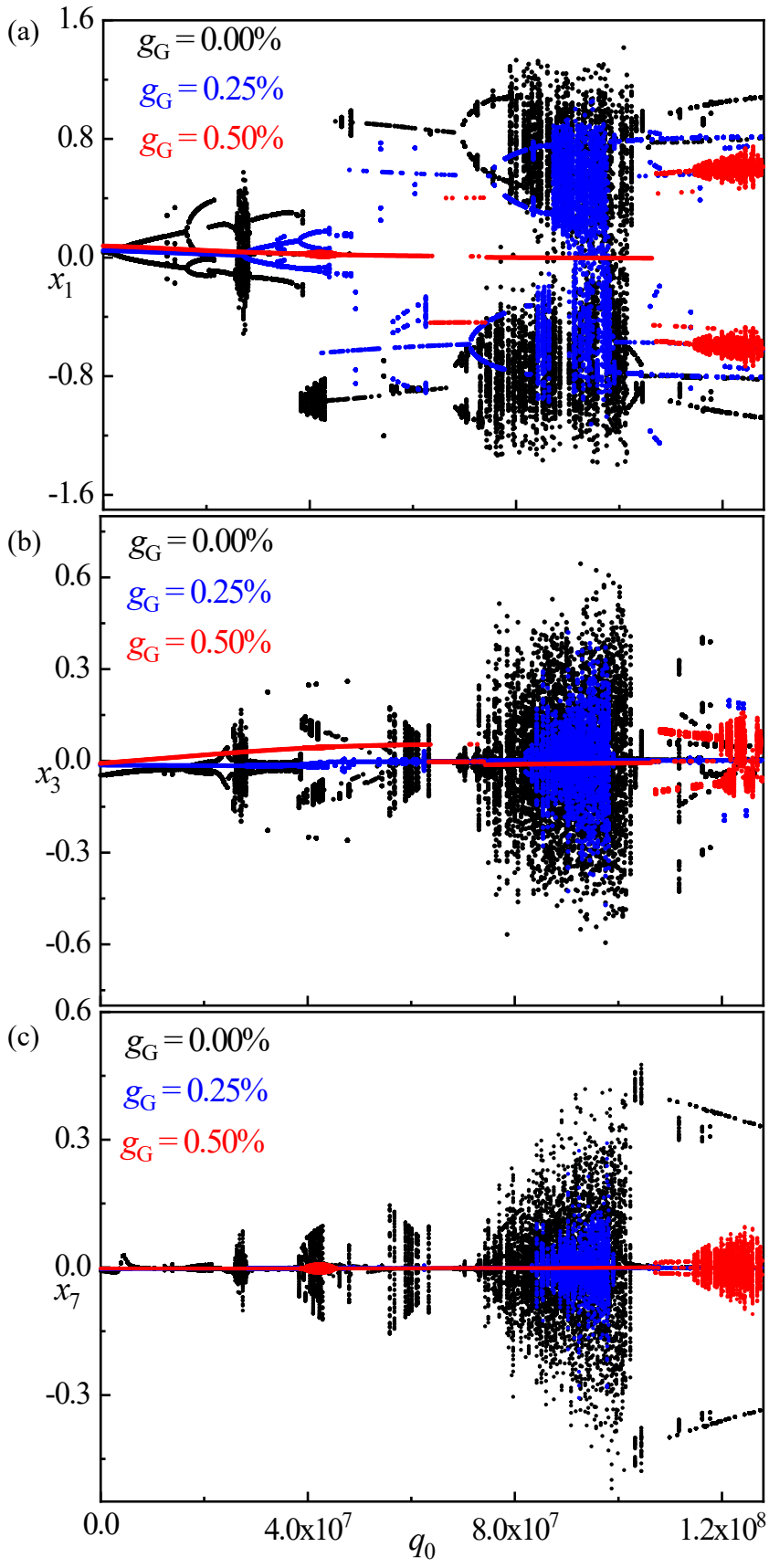
(a)
$g_G = 0.00\%$
$g_G = 0.25\%$
$g_G = 0.50\%$
1.6
0.8
0.0
-0.8
-1.6
x_1
(b)
$g_G = 0.00\%$
$g_G = 0.25\%$
$g_G = 0.50\%$
0.6
0.3
0.0
-0.3
-0.6
x_3
(c)
$g_G = 0.00\%$
$g_G = 0.25\%$
$g_G = 0.50\%$
0.3
0.0
-0.3
x_7
0.0
4.0x10^7
8.0x10^7
1.2x10^8
q_0

Figure 12

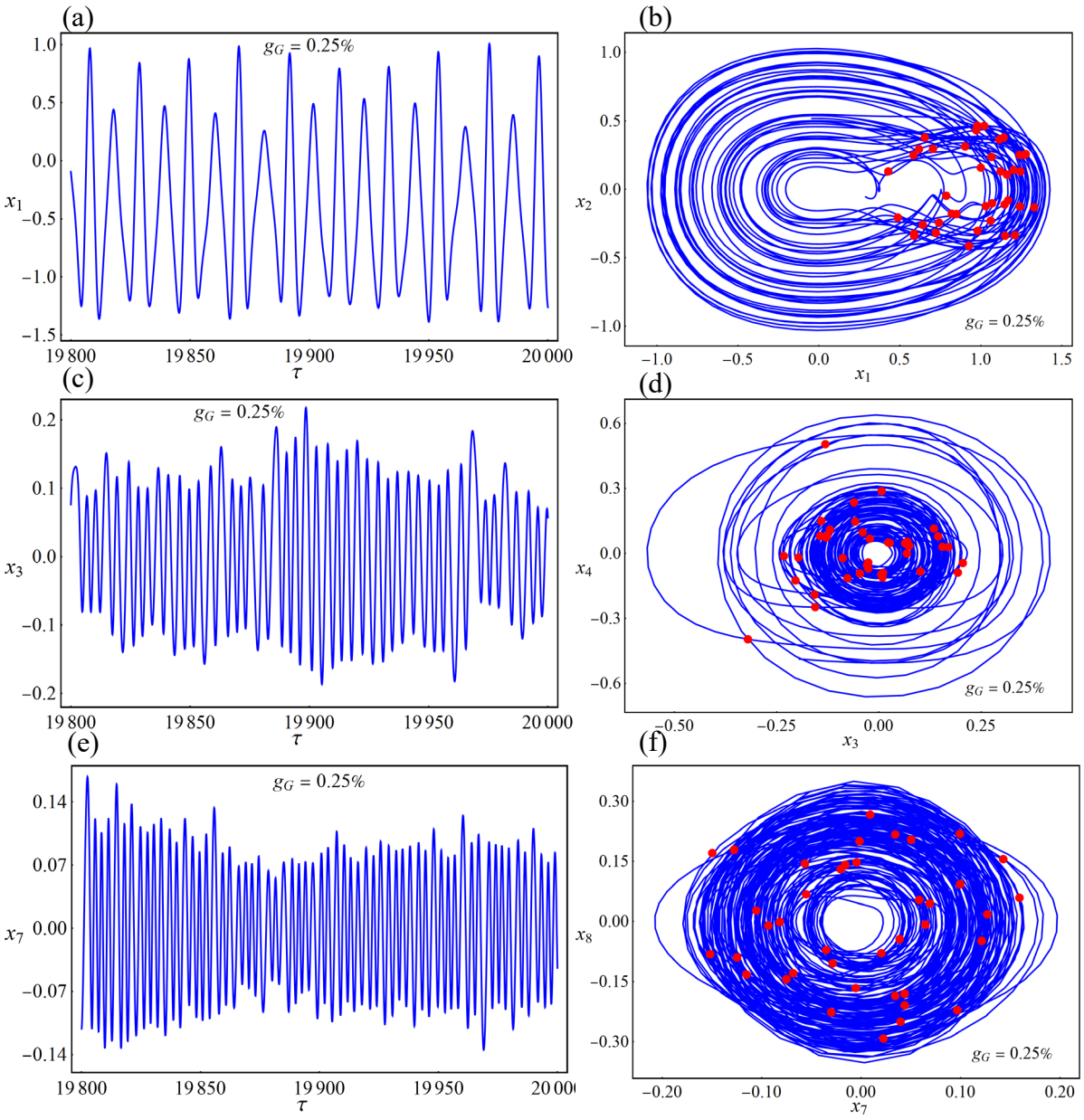
(a)
g_G = 0.25%
x_1
τ
(b)
g_G = 0.25%
x_2
x_1
(c)
g_G = 0.25%
x_3
τ
(d)
g_G = 0.25%
x_4
x_3
(e)
g_G = 0.25%
x_7
τ
(f)
g_G = 0.25%
x_8
x_7

Figure 13

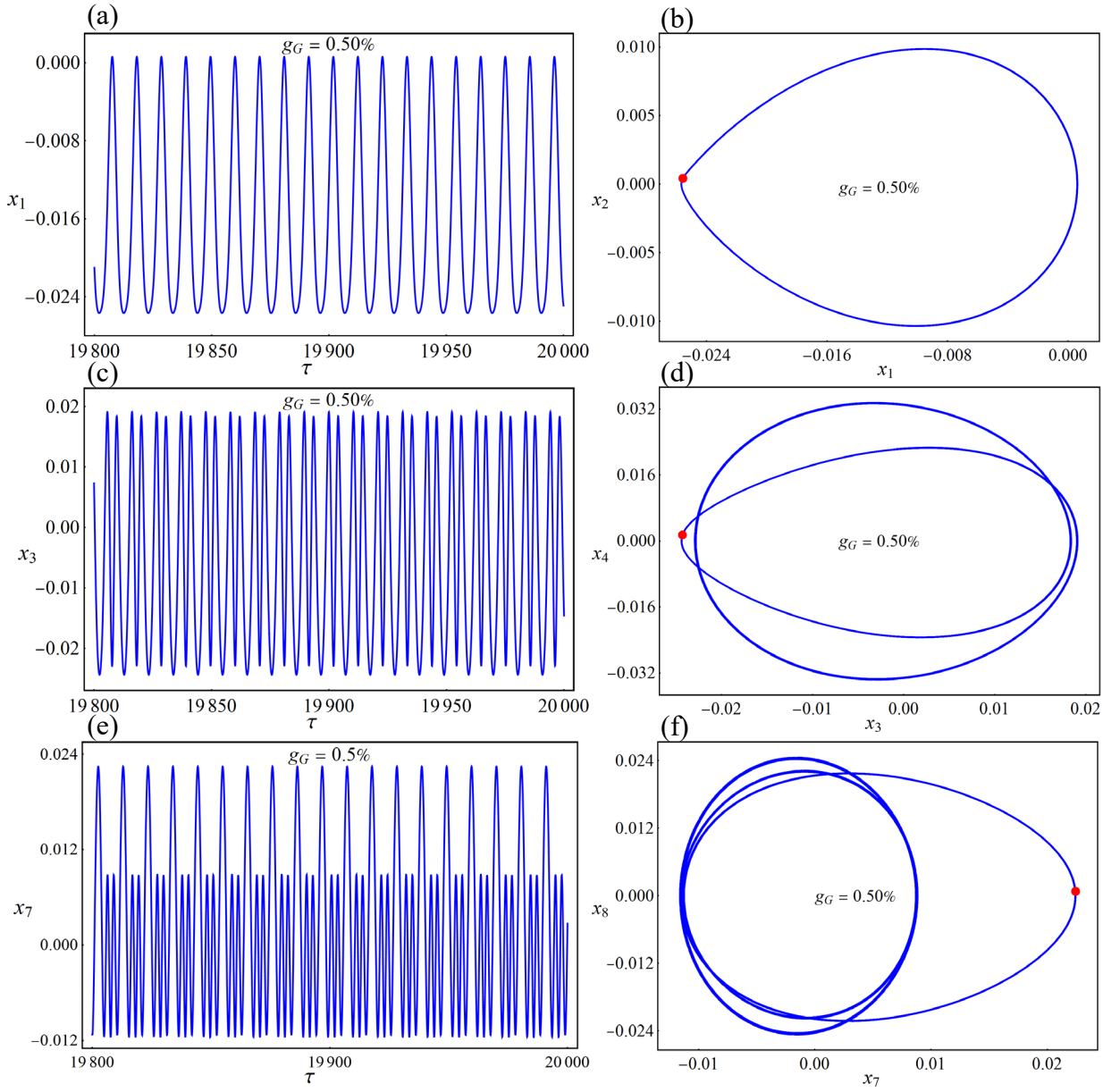
(a)
g_G = 0.50%
0.000
−0.008
−0.016
−0.024
x_1
19 800
19 850
19 900
19 950
20 000
τ
(b)
0.010
0.005
0.000
−0.005
−0.010
x_2
g_G = 0.50%
−0.024
−0.016
−0.008
0.000
x_1
(c)
g_G = 0.50%
0.02
0.01
0.00
−0.01
−0.02
x_3
19 800
19 850
19 900
19 950
20 000
τ
(d)
0.032
0.016
0.000
−0.016
−0.032
x_4
g_G = 0.50%
−0.02
−0.01
0.00
0.01
0.02
x_3
(e)
g_G = 0.5%
0.024
0.012
0.000
−0.012
x_7
19 800
19 900
20 000
τ
(f)
0.024
0.012
0.000
−0.012
−0.024
x_8
g_G = 0.50%
−0.01
0.00
0.01
0.02
x_7

Figure 14